TWO-DIMENSIONAL MODELING OF DISCHARGE SUSTAINED BY REPETITIVE NANOSECOND PULSES

by

Surya Mitra Ayalasomayajula

A Thesis

Submitted to the Faculty of Purdue University

In Partial Fulfillment of the Requirements for the degree of

Master of Science

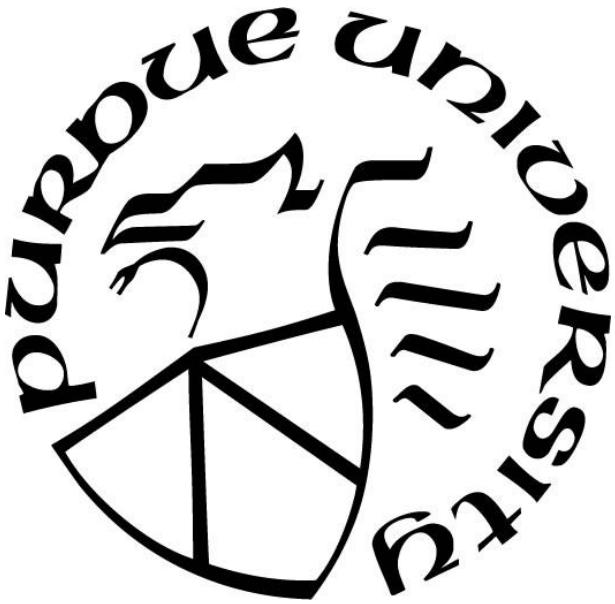

Department of Aeronautics and Astronautics

West Lafayette, Indiana

December 2018

THE PURDUE UNIVERSITY GRADUATE SCHOOL
STATEMENT OF COMMITTEE APPROVAL

Dr. Jonathan Poggie, Co-Chair
Department of Aeronautics and Astronautics
Dr. Sergey O. Macheret
Department of Aeronautics and Astronautics
Dr. Alexey Shashurin
Department of Aeronautics and Astronautics

Approved by:

Dr. Wayne Chen
Head of the Graduate Program

ACKNOWLEDGMENTS

I would like to thank my advisors Prof. Macheret and Prof. Poggie for their constant support and guidance throughout my research. Their help was invaluable throughout my masters at Purdue. I am grateful for their patience, guiding me and helping me understand the concepts of plasmas and computational modeling. I am thankful for all the meetings we had, this greatly improved my knowledge about plasmas and helped me figure out some aspects of the HPEM code. We are indebted to Prof. Mark J Kushner at University of Michigan for generously sharing his HPEM code.

I would like to thank Vladlen Podolsky and Andrei Khomenko for sharing their experimental data with me and discussing experiments with me. I would like to thank Tugba Piskin for helping me with HPEM code and discussing her work with me. I would also like to thank all my research group members for the meetings we had every week. This strengthened my knowledge and understanding of experiments in plasmas and helped me boost my enthusiasm. I would also like to thank Department of Aeronautics and Astronautics for granting me Teaching Assistantship which helped me financially for the last year. The computer resources for this work were provided by Purdue University Research Computing (RCAC).

The support and encouragement of my friends and family members has been invaluable throughout my life. I am deeply grateful to them for their emotional support and encouragement which kept me sane and helped me pursue my dreams. All this work and happiness would not have been possible if not for my mom Annapurna, my dad Suryanarayana Murty, my cousin brother Vikrant and his wife Anjali. I am deeply grateful for my dad and my cousin for their financial support during my stay at Purdue. I am indebted to Anjali and Vikrant for their warm hospitality and healthy food they provided throughout my stay at Purdue.

TABLE OF CONTENTS

LIST OF TABLES

LIST OF FIGURES

NOMENCLATURE

$(\varepsilon, \vec{r}, \theta)$	energy, position and phase in harmonic period (or time)
$f(\varepsilon, \vec{r}, \theta)$	energy distribution function ($eV^{-3/2}$)
$k_e(\vec{r}, \theta)$	electron impact rate coefficient (cm^3s^{-1})
$S_e(\vec{r}, \theta)$	electron impact source function($cm^{-3}s^{-1}$)
$k(\vec{r}, \theta)$	heavy particle collision rate coefficient (cm^3s^{-1})
$S(\vec{r}, \theta)$	heavy particle collision source function (cm^3s^{-1})
ν	collision frequency (s^{-1})
σ	conductivity ($\Omega^{-1}cm^{-1}$)
ρ	charge density (Ccm^{-3})
$\Phi_S(\vec{r}, \theta)$	electrostatic potential(V)
$E_S(\vec{r}, \theta)$	static electric field (Vcm^{-1})
$N(\vec{r})$	number density(cm^{-3})
$\vec{\phi}(\vec{r})$	flux($cm^{-2}s^{-1}$)
$T(\vec{r})$	temperature (eV or K)
EEE	Electron Energy Equation
HPEM	Hybrid Plasma Equipment Modeling
eMCS	electron Monte Carlo Simulation
FKS	Fluid Kinetic Solver
FKPM	Fluid Kinetic Poisson Module
EETM	Electron Energy Transport Module
DC	Direct Current
RF	Radio Frequency

ABSTRACT

Author: Surya Mitra, Ayalasomayajula, MS.
Institution: Purdue University
Degree Received: December 2018
Title: Two-Dimensional Modeling of Discharge Sustained by Repetitive Nanosecond Pulses.
Committee Chair: Sergey Macheret and Jonathan Poggie,

High repetition frequency nanosecond pulses have been shown to be effective in generating plasma for reconfigurable RF systems. In the present work, the focus is on simulation of nanosecond pulsed discharges in Argon at 3 Torr and interelectrode spacing of 2 cm with pulse repetition frequency of 30 kHz. The simulations have been carried out using a hybrid model, HPEM code developed by Prof. Mark J. Kushner at University of Michigan. The simulation results were compared to the experiments. Although a mismatch of results has been found, the simulations seem to capture the underlying physical phenomena. The electron temperature in the afterglow of the pulse seems to decay faster compared to the electron number density in the plasma, which is an essential feature in designing low noise plasma antennas.

1. INTRODUCTION

1.1 Objective

The objectives for the current thesis are to employ hybrid modeling to simulate a high-PRF nanosecond pulsed discharge in argon gas using the HPEM code. A two-dimensional (axisymmetric) simulation for a parallel-plate electrode setup in Argon gas with 3 ns FWHM pulse at pulse repetition frequency of 30 kHz has been performed. The simulation results were compared to the experimental results and should be able to capture the underlying physical processes. If a faster decay of electron temperature compared to the electron number density occurs after the pulse, then such plasma devices could be used for low noise plasma antennas.

1.2 Motivation

The search for the next generation of RF devices, with rapid configurability and tunability, brings us to the use of plasma for RF devices. Weakly ionized cold plasmas are attractive due to rapid switching, they can be turned on or off instantly, and they have high-tunability through variation of the conductivity and permittivity of the plasma by changing the applied voltage. There are a few obstacles in developing the plasma antennas, one of them being the thermal noise due to high electron temperatures. Maintaining the conductivity of the plasma while reducing the Johnson-Nyquist thermal noise is a challenge. Plasma sustained by high repetition nanosecond pulsed discharges could produce the required high average electron number density, while having low electron temperatures during the decay of the plasma after the pulse [5]. While the experiments provide insight into the performance of the device, an understanding of the underlying physical processes could help improve their efficiency. Modeling these plasmas is challenging, but it could help better understand the underlying physical processes.

1.3 Plasma

A plasma could be described as a quasi-neutral gaseous mixture of electrons, ions and excited neutrals co-existing with the neutral gas. The term plasma was first coined by Langmuir. Plasmas can be characterized by the average electron energies, degree of ionization, and the

average number densities of electrons and ions. The presence of charged species in plasma makes it electrically conductive, and the electrical conductivity can vary based on the charged species type and concentrations. Plasmas can be naturally occurring or manmade.

Plasmas could be generally divided into hot and cold/low temperature plasmas. Hot plasmas are plasmas having very high electron temperatures, on the order of 100 eV-1000 eV, and a very high ionization fractions, as observed in fusion devices and stars. The cold/low temperature plasmas are weakly ionized with electron temperatures ranging from 1 eV-10 eV. Generating and sustaining a hot plasma could be difficult, but a typical LTP (Low Temperature Plasma) can be generated and sustained in a lab through electric discharges. A simple setup for LTPs includes electrodes connected to a power supply and enclosed in a glass chamber filled with gas. This configuration creates plasma at room temperature based on the applied voltage and power on the electrodes. Low temperature plasmas are in a highly non-equilibrium thermodynamic state, since the electron temperatures in the plasma can be very high compared to the temperatures of the heavy particles (which are on the order of room temperature). These energetic electrons can efficiently generate radicals, charged species, excited states and photons.

LTPs operate close to room temperature while delivering a chemically rich environment, thus delivering highly reactive plasma species in a beneficial and non-destructive way to even extremely heat sensitive surfaces [9]. This feature of LTPs finds many recent technological uses. For example, the microelectronics industry is enabled by the beneficial plasma‑surface interactions which deposit and remove materials with nanometer resolution in the fabrication of microprocessors [10]. This beneficial contact with surfaces now extends to liquids, organic tissues and wounds, which led to the emerging field of plasma medicine [11]. LTPs may also non-destructively and beneficially interact with surfaces internal to the plasma, such as in a particle or aerosol-laden *dusty* plasma which has enabled, for example, nanomaterial synthesis [12]. LTPs can also be generated and sustained within liquids and bubbles in liquids, now being investigated for chemical processing, and medical applications [13]. One promising application of LTP’s is in reconfigurable RF systems.

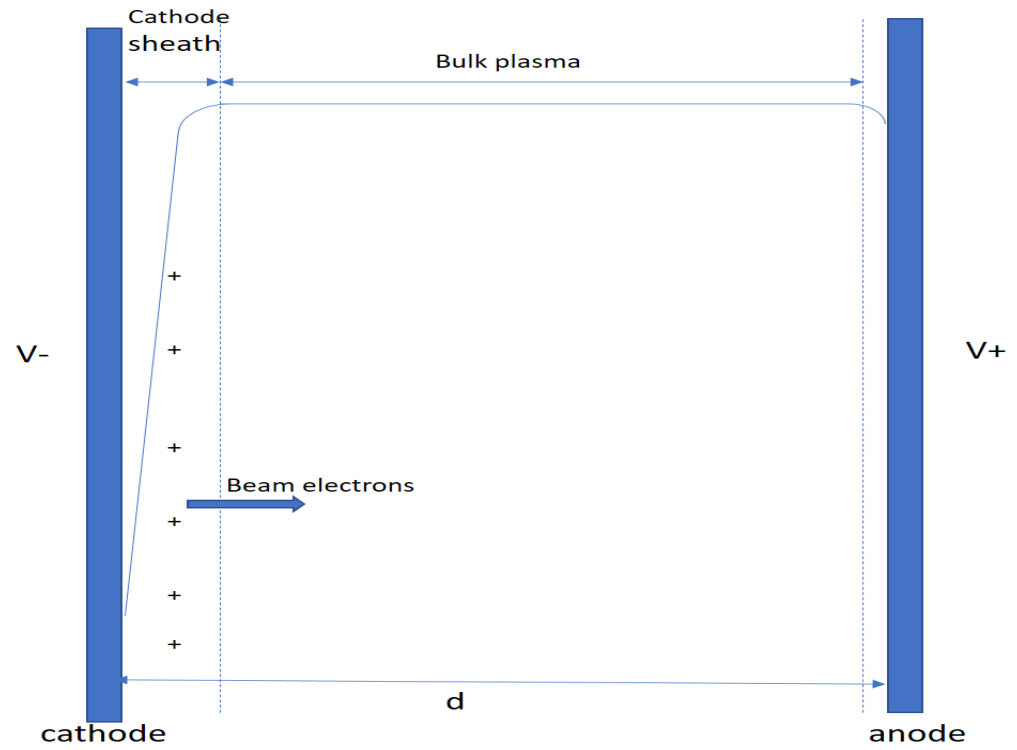

Figure 1.1: Schematic of the plasma sustained between two electrodes

1.3.1 Cathode Sheath

The simple planar electrode configuration shown in Figure 1.1 can be easily built to sustain glow discharge at room temperature. The Townsend condition must hold for a self-sustained electric discharge.

$$\int_0^l \alpha[E(x)]\,dx = \ln(1+\frac{1}{\gamma}) \tag{1.1}$$

where α is the Townsend ionization coefficient as a function of electric field E, and γ is the secondary emission coefficient. This condition reflects a balance of ion current at the cathode, due to the ionization events produced by electrons, and the electron current at the anode. This implies the ion current to the cathode should match the electron current to the anode to sustain a basic electric discharge. If the electric field were uniform throughout the plasma the self-sustainment condition would require extremely high voltage to sustain the plasma throughout the electrode gap. Instead, a lower voltage is sufficient if the potential drop is concentrated.

The ionization efficiency is higher in strong fields, so the distribution of potential would be ideal if the potential difference could be concentrated over a small region near the cathode to ensure ionization at minimum applied voltage. To sustain the current generated in the region (cathode sheath) throughout the remaining gap between electrodes, an additional voltage is only needed to compensate for losses of electrons to the anode, recombination, and attachment via weak ionization. We can exactly observe this optimization in nature; this region is called the cathode sheath. The cathode sheath is a thin region near the cathode with strong electric fields of several orders of magnitude greater than the bulk of the plasma. These strong electric fields cause majority of ionization and buildup of positive space charge in this small region near the cathode (cathode sheath).

1.3.2 Glow discharges and Plasma Tunability

The electric discharge sustained between electrodes through an applied DC voltage, can be classified into different regimes based on the voltage-current characteristics of the discharge as seen in figure 1.2.

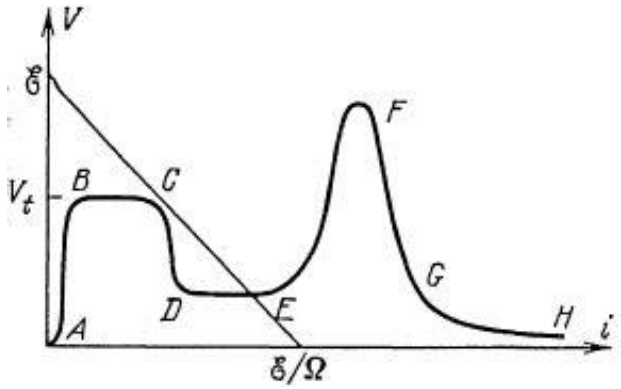

Figure 1.2: V-i characteristic of discharge sustained between electrodes for wide range of currents, (A) region of non-self-sustaining discharge, (B-C) Townsend dark discharge, (D-E) normal glow discharge, (E-F) abnormal glow discharge, (F-G) transition to arc, (G-H) arc. [*picture taken from Ref.* [8]]

Glow discharges can be normal or abnormal glow discharges. The normal glow discharge has a constant sheath thickness and operates at a constant voltage and constant current density while the discharge current in the plasma could be increased until the discharge turns into

abnormal. The voltage increases along with the current density and the discharge current in the plasma, so the sheath thickness is reduced. This feature of abnormal glow discharges enables tuning of RF circuits by changing the applied current.

Plasma sustained in between a simple electrode setup has two main regions, the sheath and the bulk plasma. These regions respond to an applied RF signal in different ways [7]. The cathode sheath consists of very few electrons and since the ions present have a very low mobility, the cathode sheath could be treated as a vacuum capacitor. The thickness of the sheath could be varied in an abnormal glow discharge regime by changing the discharge current. The bulk plasma region consists of quasi-neutral plasma, the response of this region to the RF signal could be analyzed by looking at the relative permittivity ϵ_r of the plasma.

$$\epsilon_r = \left(1 - \frac{\omega_p^2}{\omega^2 + \nu_m^2}\right) - i\left(\frac{\sigma}{\epsilon_0 \omega}\right)$$

$$\epsilon_r = \left(1 - \frac{\omega_p^2}{\omega^2 + \nu_m^2}\right) - i\left(\frac{\nu_m}{\omega}\frac{\omega_p^2}{\omega^2 + \nu_m^2}\right) \tag{1.2}$$

where σ is the electrical conductivity of the plasma, ν_m is the electron-neutral collision frequency, ω is the angular frequency of the electromagnetic wave. ω_p is the frequency of the plasma which is given by,

$$\omega_p = \sqrt{\frac{e^2 n_e}{\epsilon_0 m}} \tag{1.3}$$

e is the charge of the electron, n_e is the electron number density, ϵ_0 permittivity of free space and m is the mass of electron. The real part of the ϵ_r affects the speed and wavelength of the propagating electromagnetic wave and the imaginary part corresponds to attenuation/absorption of the wave [8]. The imaginary part is proportional to the plasma conductivity. The typical values of n_e, ω_p and, ν_m for a discharge in argon at a pressure of 3 torr are: $n_e \sim 10^{16}$ (m^{-3}), $\omega_p \sim 10^9 - 10^{10}$ (s^{-1}), $\nu_m \sim 10^9$ (s^{-1}).

It could be observed that the real part of ϵ_r is always <1, unlike the regular dielectrics where $\epsilon_r > 1$. A negative real part implies that the plasma acts as an inductor. The plasma frequency

is dependent on the electron number density and the collision frequency is dependent on the pressure and electron temperature. Thus, we can tune the plasma by varying these quantities and, in turn, varying the plasma frequency and collision frequency.

The equivalent circuit for the plasma to the RF signal has been demonstrated in Figure 1.3 [7].

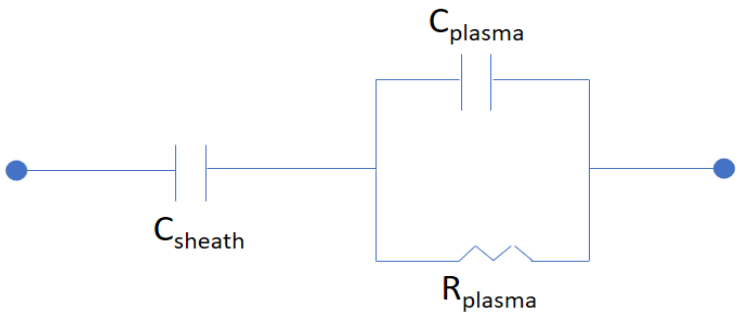

Figure 1. 3: Schematic of equivalent plasma circuit

1.3.3 Plasma Antennas and Nanosecond Pulses

Plasmas having tunable resistive, capacitive and inductive properties, making them valuable for RF electronics [7]. Through years of research, the potential advantages of plasma antennas over conventional metallic antennas have been uncovered. “Plasma antennas have been shown to be capable of being rapidly turned on and off, to withstand high powers, to have low mutual coupling in multi-element arrays, and to be frequency-reconfigurable” [5]. One of the major problems in developing plasma antennas is the presence of Johnson Nyquist thermal noise given by Eq. (1.4).

$$\frac{P_{noise}}{\Delta f} = \frac{4kT_e}{1 + \frac{\omega^2}{\nu_m^2}} \tag{1.4}$$

where P_{noise} is the thermal noise power, Δf is the bandwidth, T_e is the electron temperature, ω is the frequency of RF signal, ν_m is the collision frequency.

The Johnson Nyquist noise is proportional to electron temperature. In a plasma generated by conventional methods, reducing the electron temperature could reduce the noise, but this will in turn effect the collision frequency and the ionization of the plasma. This reduces the conductivity of the plasma which is a function of the collision frequency and electron number density:

$$\sigma = \epsilon_0 \nu_m \frac{\omega_p^2}{\omega^2 + \nu_m^2} \tag{1.5}$$

Antennas should have good electrical conductivity, and direct attempts to reduce the noise lead to a loss in performance of plasma antennas. A balance needs to be made between optimizing the thermal noise and the plasma conductivity. It has been found that plasma generated by high pulse repetition frequency nanosecond pulses could potentially solve this problem [24,5].

Nanosecond pulses could create very high electric fields during the pulse and thus cause significant ionization during the pulse. In between the pulses, the electron temperature decays faster compared to the electron number density, this feature could be exploited to create low noise plasma antennas.

1.4 Plasma Modeling

Low-temperature plasmas find application in a variety of fields. To get a complete understanding of physics governing the plasma, the required equipment may be very expensive, or the method involved may be very complex [6]. Modeling and simulation of plasmas can enhance our understanding of plasma chemistry and transport, and help develop methods for design, control and optimization of plasma processes and equipment. The synergy between modeling, simulation, and laboratory experiments is invaluable for further improving our understanding of LTPs and for developing better simulation tools with predictive capabilities over a wider range [9].

LTPs have many diversified physical processes to be addressed during modeling and simulation [6]. It is expected that a plasma model should address the fundamental plasma phenomena [1]. Different plasma models could be developed based on the simulation

conditions and the equipment design required, to capture the underlying plasma physics while each has its own advantages and limitations. We can generalize the plasma models as fluid, particle-based and hybrid models. Fluid models solve the first few moments of the Boltzmann equation, for example, the continuity, momentum and energy equations for the species. The required transport and rate coefficients for electrons, ions, and reactive species are obtained by solving the electron Boltzmann equation [3]. The Poisson equation for electric potential is coupled with the governing equations for charge carriers. The fluid or continuum models describe the averaged statistical properties of the plasma species. This approach fails at extremely low pressures or for species with low concentrations or even in the presence of large gradients or strong transient effects [6]. The fluid models might be accurate to model the bulk plasma but may not resolve some important characteristics of the plasma like the high energy electrons emitted from the cathode sheath.

Particle-based models use a statistical approach, a representative collection of particles that represent the species population are followed in space and time. The stochastic nature of elastic collisions and inelastic collisions in which particles are produced or destroyed is emulated by letting such processes happen at random times, but with an average frequency which matches the real frequency [6]. These models can accurately describe any phenomena, but are computationally intensive, and thus are limited by computational power.

The hybrid method of modeling can make use of both the fluid models and the particle-based models or can make use of different algorithms and solution procedures for different processes. In hybrid modeling we can make use of the fluid models for the bulk of the plasma and particle methods for non-local transport of high-energy beam type electrons which are emitted from the cathode. HM is a hierarchical approach to modeling where different modules are combined to accurately simulate the required conditions at hand, and run the simulation in real time [1].

For the current study, we use argon gas at a pressure p = 3 torr, with an inter-electrode gap of d = 2 cm. The electron mean free path is approximately estimated to be on the order of 90 μm. This is much smaller than the inter-electrode distance, so a fluid model could be applied for the bulk of the plasma. Secondary electrons produced at the cathode, and accelerated in the sheath to high energy, will be injected into the bulk plasma, and be active in ionization deep inside that bulk plasma since the energy relaxation length of the electrons is on the order of a

few millimeter approximately 0.7cm. This non-local behavior of beam type electrons requires particle-based modeling. So, the current study requires hybrid modeling for simulation.

2. METHODOLOGY

2.1 Hybrid Modeling and HPEM

Plasma modeling is computationally intensive, a direct integration of coupled sets of differential equations addressing all the phenomena will be extremely challenging. Hybrid modeling (HM) is an efficient plasma modeling technique to address both fundamental physics and practicality of equipment design, while striking a balance between computation time and physical accuracy. HM is a hierarchical approach to modeling whose goals include integration of diverse, first principles physics modules which can be implemented over a large enough dynamic range in time to be relevant to equipment modeling [1].

The Hybrid Plasma Equipment Model (HPEM) is developed by Prof. Mark Kushner at the University of Michigan. HPEM is built on the principles of Hybrid Modeling. It is used to model low temperature plasmas for equipment design. As mentioned earlier, a direct integration of the coupled sets of differential equations could be computationally intensive and may not be practical to implement and address different phenomena. HPEM consists of different modules pertaining to different physical processes. The physics in each module is compartmentalized to work independently; this allows for the use of different algorithms to represent the same physical processes. In this manner, the modules and algorithms best suited for the conditions of interest can be used without affecting other modules. The user can turn off the modules which are not deemed to be important, and can also choose from different algorithms to best solve the problem at hand. These modules exchange information in a hierarchical manner. There is a need to resolve a wide range of time scales for different processes involved, for example the dynamic time scale for fluid module is on the order of 10 μs whereas that for the electron energy transport module is on the order of 1 μs. HPEM determines the relative time scales of integration within the modules to resolve the physics and the time for exchange of information between modules. In each iteration, HPEM cycles through all the active modules and the vastly disparate time scales in the modules are iteratively combined using time-slicing techniques. This allows for the best representation of the physical processes.

This work made use of the Fluid Kinetic Poisson Module (FKPM) and Electron Energy Transport Module (EETM) modules of the HPEM for this study. These modules communicate as shown in Figure 2.1.

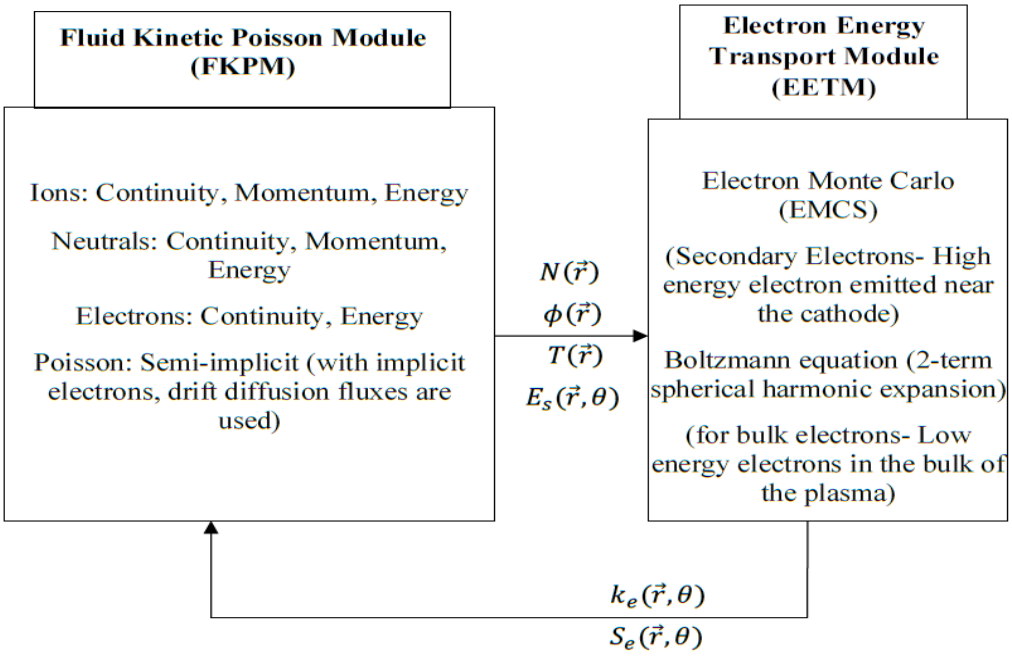

Figure 2. 1: HPEM modules used and execution path.

Table 2. 1: Estimated order of values of space and time scales for the present simulation.

Electron mean free path: $\lambda_e = \frac{1}{\pi d^2 N_{Ar}}$ d= radius of argon atom.	~ 90 µm
Diffusion length scale (Λ): $\frac{1}{\Lambda} = \sqrt{\left(\frac{2.4}{R}\right)^2 + \left(\frac{\pi}{L}\right)^2}$	~ 0.6 cm
Characteristic diffusion time for species i (τ_i): $\tau_i = \frac{\Lambda^2}{D_i}$	for electrons ~ 10^{-7} s for heavy particles ~ 10^{-2} s
Dielectric relaxation time (Δt_d): $\Delta t_d = \frac{\epsilon_0}{\sigma}$	~ 10^{-11} s
Drift Velocity: $v_d = \frac{\Lambda}{\Delta t_d}$	for electrons ~ 6.10^6 (cm/s) for heavy particles ~ 60 (cm/s)
CFL criteria (Δt_c): $\Delta t_c \leq \frac{\Delta z}{v_d}$	for electrons ~ $10^{-9} - 10^{-10}$ (s) for heavy particles ~ $10^{-5} - 10^{-6}$ (s)

2.2 Fluid Kinetic Poisson Module (FKPM)

The continuity, momentum and energy equations are solved in fluid kinetics-Poisson module (FKPM) to produce densities, momenta, and temperatures of neutral and charged species. Due to the tight coupling of electrostatic fields to the densities of charged particles, the solution of Poisson's equation for the electrostatic potential $\Phi_s(\vec{r},\theta)$, is performed within the FKPM. The FKPM accepts $kS_e(\vec{r},\theta)$ as inputs from EETM, to output the densities $N(\vec{r})$, fluxes $\phi(\vec{r})$ and temperatures $T(\vec{r})$ (collectively abbreviated as $N\phi T(\vec{r})$, of neutral and charged species; and electrostatic potential $\Phi_s(\vec{r},\theta)$ which provides the electrostatic field $E_s(\vec{r},\theta)$, in addition to reaction rate coefficients $k(\vec{r},\theta)$, and source functions $S(\vec{r},\theta)$ of heavy particles.

2.2.1 Ions and Neutrals.

We choose to use full hydrodynamic conservation equations in the FKPM for our simulation [14,15]. The continuity, momentum, and energy equations are solved for all particles. The continuity equation

$$\frac{\partial N_i}{\partial t} = -\nabla.\overrightarrow{\phi_i} + S_i \tag{2.1}$$

where N_i, $\vec{\phi}_i = N_i\vec{v}_i$, and S_i are the species density, flux, and source for species *i*. The first term on the left-hand side of Eq 2.1 represents the rate of change of number density in a control volume, while the first term on the right-hand side represents the net flux of species *i* entering the control volume and the second term represents the production or loss of species *i* in the control volume.

The conservation of momentum equation is solved to produce the $\vec{\phi}_i$ flux of heavy particles.

$$\frac{\partial(N_i\vec{v}_i)}{\partial t} = -\frac{1}{m_i}\nabla(N_i kT_i) - \nabla.(N_i\vec{v}_i\vec{v}_i) + \frac{q_i}{m_i}N_i\left(\overrightarrow{E_S}\right) - \nabla.\bar{\bar{\nu}}_i - \sum_j \frac{m_j}{m_i+m_j}N_iN_j\left(\vec{v}_i-\vec{v}_j\right)\nu_{ij} \tag{2.2a}$$

where $\vec{v}_i$ is the velocity, $\bar{\bar{\nu}}_i$ is the viscous stress tensor (used only for neutral species) and ν_{ij} is the collision frequency between species *i* and species *j*. The last term of the equation accounts for the momentum losses due to collisions with species *j*. The first term on the left-hand side of Eq 2.2a represents the net acceleration of species in a control volume, while the first term

on the right hand side represents the force due to the pressure gradient, the second term represents the acceleration created due to the flux of particles *i* on the control volume, the third term represents the acceleration due to the static electric field (for current study no magnetic fields or non-conservative electric fields are included), the fourth term represents the viscous forces on the control volume and the last term is the change in momentum of species *i* due to collision with species *j*. [14]

The drift-diffusion equation is used for electron flux Eq 2.2b,

$$\vec{\phi}_e = -D_e \nabla(N_e) + q_e \mu_e N_e \left(\overrightarrow{E_S}\right) \tag{2.2b}$$

The energy equation is solved to obtain the temperatures and number densities of the ions and neutral species.

$$\frac{\partial (N_i \varepsilon_i)}{\partial t} = -\nabla.(\bar{\bar{\kappa}} \nabla T_i) - P_i \nabla . \overrightarrow{v_i} - \nabla . (N_i \overrightarrow{v_i} \varepsilon_i) + \frac{N_i q_i^2}{m_i \nu_i} E_S^2 - \overline{\overline{\nu_i}} . \nabla \vec{v}_i - \sum_{m,j} k_{mij} N_i N_j \varepsilon_i + \sum_{m,j,l} k_{mjl} N_i N_j \Delta \varepsilon_{mjl} \tag{2.3a}$$

where ε_i is the total energy, $\bar{\bar{\kappa}}_i$ is the thermal conductivity, P_i is the partial pressure, and T_i is the temperature of the species. The rates of reactions for heavy particles (neutrals and ions) could be entered in Arrhenius format during the input and the electron impact rate coefficients and source functions are calculated in the EETM module.

The term on the left-hand side of Eq 2.3 represents the net change in energy of species *i* in a control volume, while the first term on the right hand side represents the net flux of heat into the control volume through conduction, the second term represents (compressive heating) the work done by the pressure in heating the control volume, the third term represents advective transport i.e., the net flux of heat into the control volume by particle *i*, the fourth term represents joule heating the work done by static electric field (for current study no magnetic fields or non-conservative electric fields are included) in heating the control volume, the fifth term represents viscous dissipative heating due to the viscosity (effects neglected for charged species), the sixth term implies all the reactions *m* of species *i* with species *j* having rate coefficient k_{mij} which result in removal of species *i* produces a loss of energy for species *i* of ε_i per event, the last term implies all the reactions *m* of species *l* with species *j* having rate

coefficient k_{mjl} which result in formation of species i produces energy for species i of $\Delta\varepsilon_{mjl}$ per event. The last two terms tend to account for change in enthalpy in a non-conventional manner.

The bulk electron energy transport is addressed by time integration of the electron energy equation

$$\frac{\partial\,(\frac{3}{2}n_e kT_e)}{\partial t} = P - L(T_e) - \nabla.\left(\frac{5}{2}\phi_e kT_e - \bar{\bar{\kappa}}(T_e).\nabla T_e\right) + P_{EB} \tag{2.3a}$$

P is the power deposition from electrostatic field, P_{EB} is the power transferred from slowing beam type electrons to the bulk distribution, and L is the power loss due to collisions. The electrostatic heating is given by collisional Joule heating $P = q_e\vec{\phi}_e.E$. Isotropic transport coefficients and electron impact rate coefficients were obtained from solution of Boltzmann equation using a 2-term spherical harmonic expansion approximation.

2.2.2 Poisson Solver

The tight coupling of charged particle densities and electrostatic fields requires Poisson's equation for the electrostatic potential Eq (2.4) to be solved in the FKPM.

$$\nabla.\vec{E}_S = \frac{\rho}{\epsilon_0} \quad ; \quad \nabla.(\nabla\Phi_S) = \frac{\rho}{\epsilon_0} \tag{2.5b}$$

For the current study, we solve the Poisson semi-implicitly with implicit electron densities and fluxes i.e., the Poisson equation is solved for a future time using an incremental prediction of charge densities based on the divergence of their fluxes provided by drift-diffusion expressions. The appearance of potential in the drift-diffusion fluxes provides a degree of implicitness [2].

$$-\epsilon_0\nabla.\nabla\Phi_S(t+\Delta t) = \sum_i q_i\left[N_i(t) - \Delta t\nabla.\overrightarrow{\phi_i}\left(\Phi_S(t+\Delta t)\right) + S_i(t)\right] + \rho_s(t) - \Delta t\nabla.\left(\sum_i q_i\overrightarrow{\phi_{si}}\left(\Phi_S(t+\Delta t)\right) - \sigma_M\nabla\Phi_S(t+\Delta t)\right) \tag{2.5a}$$

$$\vec{\phi}_i = -D_i\nabla(N_i) + q_i\mu_i N_i(\nabla\Phi_S) \tag{2.5b}$$

$$n_e(t+\Delta t) = n_e(t) - \nabla.\overrightarrow{\phi_e}\left(\Phi_S(t+\Delta t)\right) + S_e(t) \tag{2.6}$$

where $\rho_s(t)$ is the charge density in or on non-plasma materials, ϕ_{si} is the flux of charged species incident onto surfaces in contact with plasma, σ_M is the material conductivity. This treatment of semi-implicit Poisson equation with implicit electrons allows us to get rid of the limitations on time step (Δt) caused by the dielectric relaxation time [2]. The method of successive over relaxation (SOR) is used with incomplete LU Biconjugate gradient sparse Ax=b solver for the implicit solution of the Poisson equation. The convergence criteria for the Poisson solver is $\frac{\Phi_s - \Phi_{s,old}}{\Phi_s} \leq 10^{-4}$. The boundary conditions for the Poisson's equation depend on the surface (metallic or dielectric); for a metallic surface the boundary value of the potential is specified by the surface potential.

2.3 Electron Energy Transport Module (EETM)

The electron energy transport module solves for the electron impact rate coefficients $k_e(\vec{r},\theta)$ and electron impact source functions $S_e(\vec{r},\theta)$, taking as inputs the electrostatic field $E_s(\vec{r},\theta)$ and the number densities $N(\vec{r})$ from the FKPM. Due to the implementation of secondary electron emission in the present calculations, there are two types of electrons. These two types need to be treated differently. The energy distribution functions for low-energy bulk electrons are computed using the 2-term spherical harmonic approximation to the Boltzmann equation (BE). The secondary electrons, which act as high energy beam type electrons, are modeled using electron Monte Carlo Simulation (eMCS). For computational efficiency, interaction between these two types of electrons is neglected here. The energy scale for both sets of calculations is discretized into 5 ranges 0 eV - 5 eV, 5 eV - 12 eV, 12 eV – 50 eV, 50 eV – 100 eV, 100 eV - 2000 eV with each range divided into 100 bins.

2.3.1 Boltzmann Solution and Electron Energy equation

The Boltzmann equation is implicitly solved with a two-term spherical harmonic expansion. The equation is discretized in energy space using the energy spacing described above. The electron impact and transport coefficients are generated as functions of E/N. These results are translated into a table of transport coefficients vs the mean electron energy for a given selection of E/N values [3], to be utilized in the FKPM module. The electron energy equation is integrated implicitly in time in the FKS to provide electron temperature.

2.3.2 Electron Monte Carlo Simulation (eMCS)

Electron Monte Carlo simulations integrate the electron trajectories based on the electromagnetic fields obtained from the Electromagnetics module (EMM) and the static electric fields obtained from the Fluid kinetics module (FKM) and employs Monte Carlo techniques for collisions with heavy particles (neutrals and ions) and electrons [4]. In the beginning of eMCS, initial velocities are assigned for electrons from a Maxwellian EED. The positions in the reactor are assigned using a distribution weighted by the local electron density obtained in the FKM. On subsequent calls to the eMCS the trajectories are restored from their coordinates at the end of the previous call to the eMCS. The pseudo-particle trajectories are advanced by solving the Lorentz equation and the equation of motion by a second order Euler method.

$$\frac{\partial \overrightarrow{v_e}}{\partial t} = \frac{q_e}{m_e}\left(\vec{E} + \overrightarrow{v_e} \times \overrightarrow{B}\right)$$
$$\frac{\partial \overrightarrow{r_e}}{\partial t} = \overrightarrow{v_e} \tag{2.7}$$

where $\vec{v}_e, \vec{E}\ and\ \vec{B}$ are the local velocity, electric field, and magnetic field respectively.

The electron energies of interest are discretized into 5 energy ranges and binned, as mentioned earlier. The energy bins have a constant width over a specified energy range to simplify the collection of statistics and collisional frequencies. Within a given energy bin *i*, the total collisional frequency ν_i is computed by summing all possible collisions with heavy particles.

$$\nu_i = \left(\frac{2\epsilon_i}{m_e}\right)^{0.5} \sum_{j,k} \sigma_{ijk} N_j \tag{2.8}$$

where ϵ_i is the average energy within the ith bin, σ_{ijk} is the cross section at energy *i*, for species *j* and the collision process *k*, and the N_j is the number density of species *j*.

Not all particles participate in collisions so the non-colliding particles need to have a constant collision frequency until they collide. This is accomplished by adding an additional fictitious process referred to as a null collision such that all electrons within a given energy range appear

to have the same collision frequency. The null collision frequency at an energy ε_i in energy range j is given by, $\nu_{nij} = \nu_{mj} - \nu_i$, where ν_{mj} is the maximum collision frequency based on both electron energy and density of collision partners. Separate maximum collision frequencies and null collision frequencies are used for subintervals of the energy distribution to minimize the occurrence of null collisions and the time between collisions can be obtained.

The type of collision is determined by generating a random number r_1 on (0,1). If $r_1 \leq {}^{\nu_{nij}}/_{\nu_{mj}}$ then the electron collision is null, and the electron trajectory is unhindered. For a real collision, we find the particular electron collision j which satisfies $\frac{1}{\nu_{mj}}\sum_{k=1}^{n-1}\nu_k < r_2 \leq \frac{1}{\nu_{mj}}\sum_{k=1}^{n}\nu_k$, where all collision frequencies are computed based on the maximum density of collision partner for process n. This requires another null check based on the local density of the collisional partner. For an ionizing collision a secondary electron is added to the simulation at the same location as the primary particle, and with a randomly chosen isotropic angular distribution. After determining the type and nature of collision, the electron energy is reduced, and the trajectory is scattered. The final velocities are determined by applying the scattered matrix. The energy distribution functions can be obtained. The inclusion of null collisions allows eMCS to accurately simulate non-local effects.

For the present conditions, only the secondary electrons are treated as beam-type electrons and eMCS needs to be applied for these electrons. A similar approach mentioned above is followed for the solution, with a few changes. The initial positions of the electrons are not determined by bulk plasma; instead, the flux of energetic particles of type j striking the surface $\phi_j(\vec{r})$ is derived from FKS. The total rate of secondary emission is obtained from:

$$R_S = \sum_k R_{Sk} \qquad R_{Sk} = \sum_j \gamma_j \phi_j(\vec{r_k})\, A_k \tag{2.9}$$

where the summation is over the species j having secondary emission coefficient γ_j and surface locations k having surface area A_k. A preselected number of secondary electrons are randomly launched perpendicular to the surface with an energy equivalent to the work function of the material at spatial location k in proportion to ${}^{R_{Sk}}/_{R_S}$. Particle trajectories are the tracked, and the statistics are collected to produce the distribution functions $f_s(\varepsilon, \vec{r})$. The trajectories of

pseudo particles are followed until the particle strikes a surface, or falls below a specified energy after which the particle is removed from the simulation.

Since $f_s(\varepsilon, \vec{r})$ is normalized to the magnitude of secondary electron current R_S, only electron impact source functions due to secondary electrons are transferred back to the FKS.

$$S_{ej} = N_j(\vec{r}) \sum_{i=1} f_{si}(\vec{r})\, \sigma_j(\varepsilon_i) \left(\frac{2\varepsilon_i}{m_e}\right)^{0.5} \Delta\varepsilon_i \qquad (2.10)$$

The source functions from secondary emission are incorporated, along with the electron impact ionization rates and sources obtained by solving Boltzmann Electron energy equation for the Bulk electrons in the FKS. For the present calculations, the e-e collisions and the heating of bulk electrons due to the secondary electrons are neglected to reduce computation time.

2.4 Time dependence

Plasma modeling in a non-modular approach (a tightly-coupled approach) has no ambiguity on time dependence, since all processes are integrated simultaneously as one large set of partial differential equations. In hybrid modeling, however, different modules may resolve different timescales. HPEM uses time slicing techniques to resolve a wide range of time scales. In time slicing, a given module integrates its respective equations in time, and during this integration the quantities received from other modules remain time-invariant, or are allowed to vary in time in a predetermined way. The HPEM code decides the time spent is any module based on its dynamic time scale.

In time slicing between FKPM and EETM, some knowledge of the changes in mole fractions or E/N that can produce a significant change in the $Sk_e(\vec{r}, \theta)$ is required. When these changes in mole fraction or E/N exceed a certain limit the $Sk_e(\vec{r}, \theta)$ values need to be updated. These changes can be user specified or automatically decided by the code. For the current simulation, the sequence might consist of an initial call to the EETM to provide starting values of $Sk_e(\vec{r}, \theta)$. The densities are time integrated in the FKPM until the change in mole fractions or *E/N* exceeds a threshold value. At that time, the new densities and *E/N* are transferred back to the EETM to update the electron impact rate coefficients and source functions. As the time integration approaches the steady state, the frequency with which the EETM is called decreases [1].

3. COMPUTATIONAL SETUP, CONVERGENCE AND GRID RESOLUTION

The current work aims at computationally modeling experiments on high voltage nanosecond pulse discharges with high repetition frequency in HPEM. The experimental setup under investigation is explained in section 3.1, and the results obtained are discussed. Section 3.2 discusses setting up the computations and post processing, Section 3.3 discusses the computational resolution, and Section 3.4 discusses the restart features of the HPEM code and simulation of the pulse repetition.

3.1 Experimental Setup and Results

The experiments simulated here were carried out in a sealed chamber [5], with two aluminum parallel plate electrodes, 10.16 cm in diameter, and separated by 2 cm as shown in Figure 3.1. The chamber was filled with Argon at a pressure of 3 Torr. The plasma was generated using a FID FPG 1-3MH2 pulser. The pulser outputs a fixed 820 V, 3 ns FWHM pulse at pulse repetition frequency up to a maximum of 3 MHz [5]. Tests were performed with pulsed repetition rates from 30-75 kHz. We consider the results at a pulse repetition frequency of 30 kHz for comparison with the computations. During the experiment, the voltage and current profiles were measured using a back current shunt. The time-resolved average electron number density in the plasma was obtained by microwave interferometry [5]. The plots of voltage and current during the pulse and the plots of average electron number densities from the experiment are shown in Figure 3.2a and 3.2b respectively.

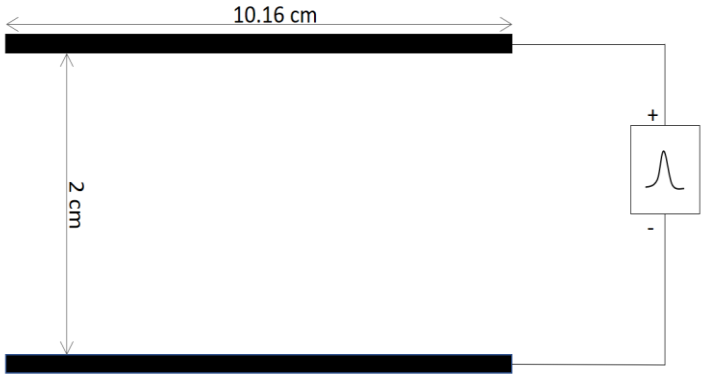

Figure 3.1: Simplified schematic of the experimental setup

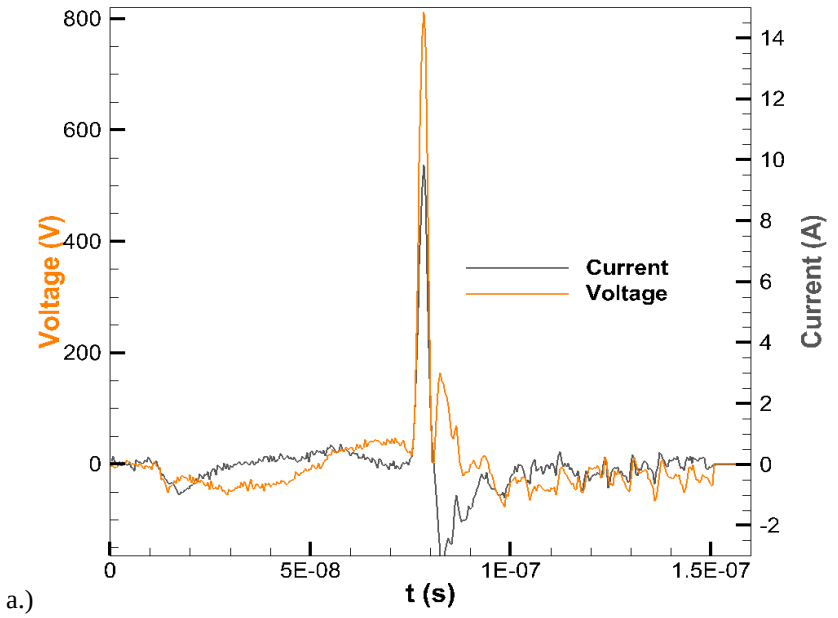

a.)

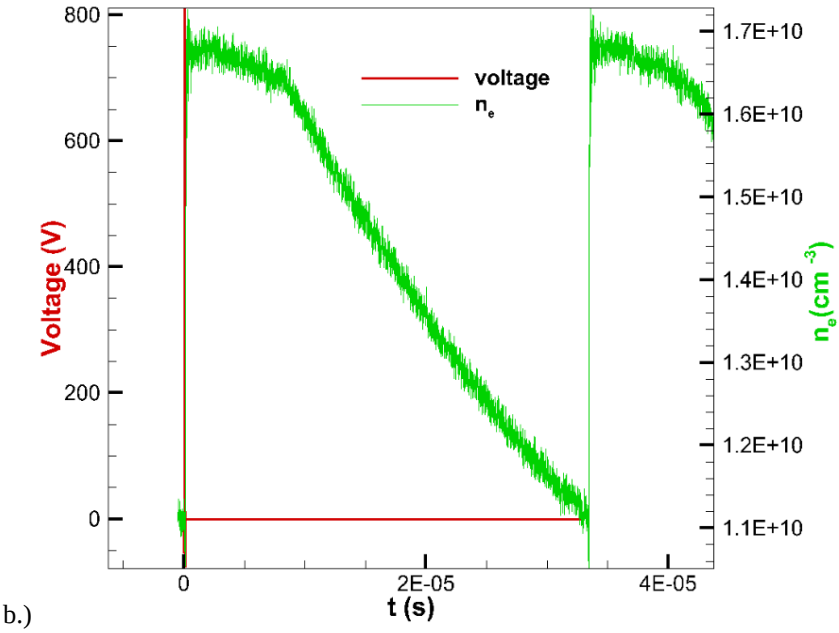

b.)

Figure 3.2: a) Plot of the DC voltage pulse applied and the measured current in the plasma. b) Electron number density measured from microwave interferometry

3.2 Simulation Setup

3.2.1 Simulation Domain

The simulation domain setup has been shown in Figure 3.3. The domain has been simplified, but was chosen to resemble the experimental conditions as closely as possible. Like the experiments, the anode is the powered side whereas the cathode is grounded. The entire domain consists of different regions: the plasma zone, the metal electrodes, dielectric, and the metal encasing the entire setup. HPEM requires the user to specify different zones for creating the mesh and to apply different materials to those zones. The cells in the plasma zone are assigned to be the gas and plasma. HPEM uses the edges of this plasma zone to set the required boundary conditions. It is essential that the plasma zone is surrounded by a solid boundary (metals or dielectrics) for proper functioning of the code. Also, the entire simulation setup in HPEM needs to be encased in a metal boundary.

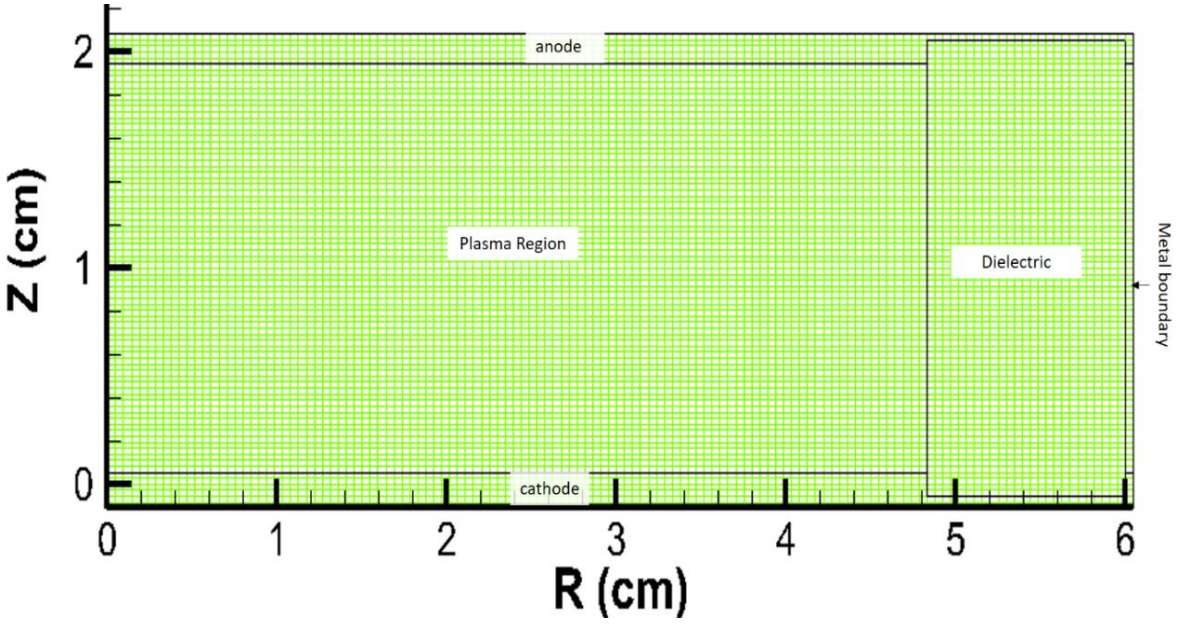

Figure 3.3: The simulation domain and mesh setup.

3.2.2 Initialization and HPEM Outputs

In setting up the simulation, the initial number densities of the species (except the electron number density) are unknown. The electron number density measured in the experiments is specified for the initial electron number density, and the charged species number densities are

chosen so the plasma is quasi-neutral. The species and reaction data set included are listed in appendix A. At the start of the simulation, all the species were distributed in the plasma domain using an exponential distribution. The secondary emission coefficient is set to a constant value of 0.15.

HPEM outputs a Tecplot format data file containing the domain averaged values of the species densities, temperatures, and plasma potential as a function of time. The data from this output file is used for comparison in this thesis. HPEM also outputs the 2D-data at every iteration of the simulation in Tecplot format. This is used for calculating the current.

3.3 Computational resolution

3.3.1 Time resolution

To examine the sensitivity of the simulation results to the magnitude of the time step used during the pulse, for a given grid resolution of 225x66 (N_z x N_r) in the z-direction and r-direction, different time steps are chosen below 0.4 ns and the cases are checked for temporal convergence. The values of average electron number densities are compared as shown in Figure 3.4. There is a maximum variation of 0.85% in electron number density observed with time steps of 0.4 ns compared with other time steps. We can conclude that the code converges in time with a time step of 0.4 ns, at least for spatially averaged values.

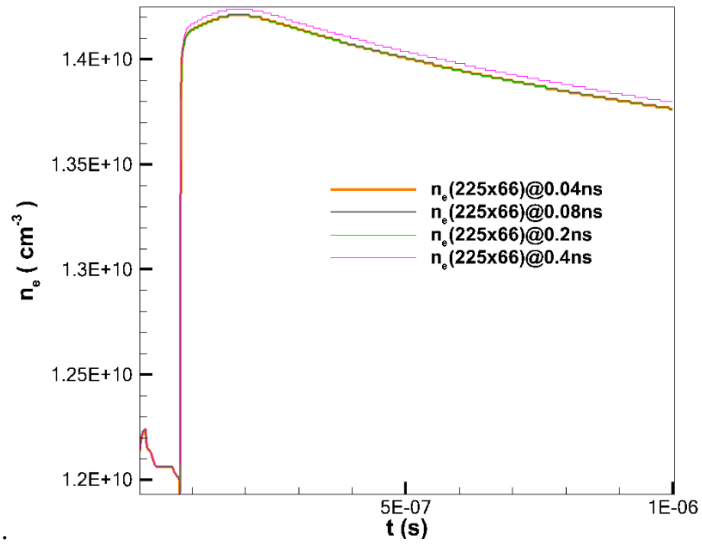

Figure 3.4: Plots of average electron number density vs time during the pulse with different time steps.

3.3.2 Spatial resolution

HPEM code limits the grid resolutions to a maximum of 900x262 (N_z x N_r). The sensitivity of the results to the grid resolution has also been investigated. The time step of 0.4 ns is used for different grid resolutions: 112x33, 225x66, 450x131 and 900x262. The average electron number densities are compared to check for convergence as shown in Figure 3.5.

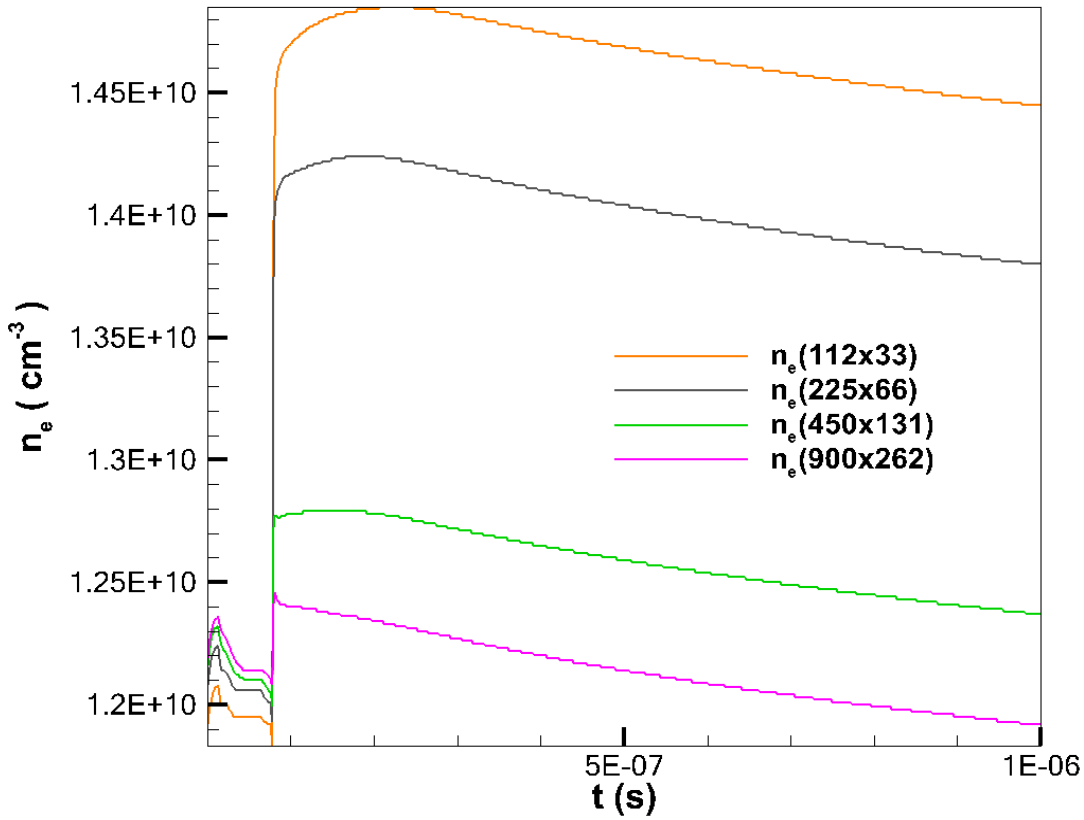

Figure 3.5: Plots of the average electron number density for different grid resolutions (N_z x N_r)

Richardson extrapolation has been applied to these results to obtain the converged solution. The accuracy of the methods should increase as the grid spacing is decreased to zero. The Richardson extrapolation involves running the simulations on two or more finer grids and extrapolating these values to obtain an approximate solution with zero grid spacing [31].

Richardson extrapolation was implemented over the 3 different grid resolutions f_1 (900×262), f_2 (450×131), f_3 (225×66) since the average electron number density values seem

to converge for these grid resolutions. f_1 is the value of the function on finest of the three grids, the grid spacing is so chosen that the f_1 has half the grid spacing as f_2 and f_2 has half the grid spacing as f_3 in both Z and R directions. This choice of grid spacing ensures a constant change in area of the unit cell from f_1 to f_2 to f_3.

$$f_1 = f_{ext} + a\Delta_1^p \;\; ; \;\; f_2 = f_{ext} + a\Delta_2^p \;\; ; \;\; f_3 = f_{ext} + a\Delta_3^p \tag{3.3}$$

where, f_{ext} is the exact value of the function with zero grid spacing, Δ_i is the area of the unit cell for the chosen grid resolution i,.and a and p are the scaling factors. Since we have three equations (Eq. 3.3) and three unknowns a, p and f_{ext} we can solve these equations and obtain the f_{ext} value as follows.

$$p = \ln\left(\frac{f_3 - f_2}{f_2 - f_1}\right) \Big/ \ln(r) \qquad where, \qquad r = \frac{\Delta_3}{\Delta_2} = \frac{\Delta_2}{\Delta_1} = 4 \tag{3.4}$$

$$a = \frac{f_2 - f_1}{\Delta_2^p - \Delta_1^p} = \frac{f_3 - f_2}{\Delta_3^p - \Delta_2^p} \tag{3.5}$$

$$f_{ext} = f_1 - a\Delta_1^p \tag{3.6}$$

$$\frac{1}{R} = \frac{f_3 - f_2}{f_2 - f_1}$$

The convergence ratio R could be determined for the type of convergence observed. A monotonic convergence is observed when 0<R<1 and oscillatory convergence for R<0 and divergence for R>1. The plot of R (Figure 3.6a) shows divergence and oscillatory convergence below 2e-7 s. This is evident in the extrapolated values for the average electron number density is shown in Figure 3.6b shooting up to very high values below 1e-07 s. This could be due to the choice of time step for the finer grid. A simple estimate shows that the courant limit is not satisfied for the given grid resolution of 900 points in N_z and time step of 0.4ns. Our attempts to decrease the time step and run the simulation were unsuccessful due to extremely unreasonable run times.

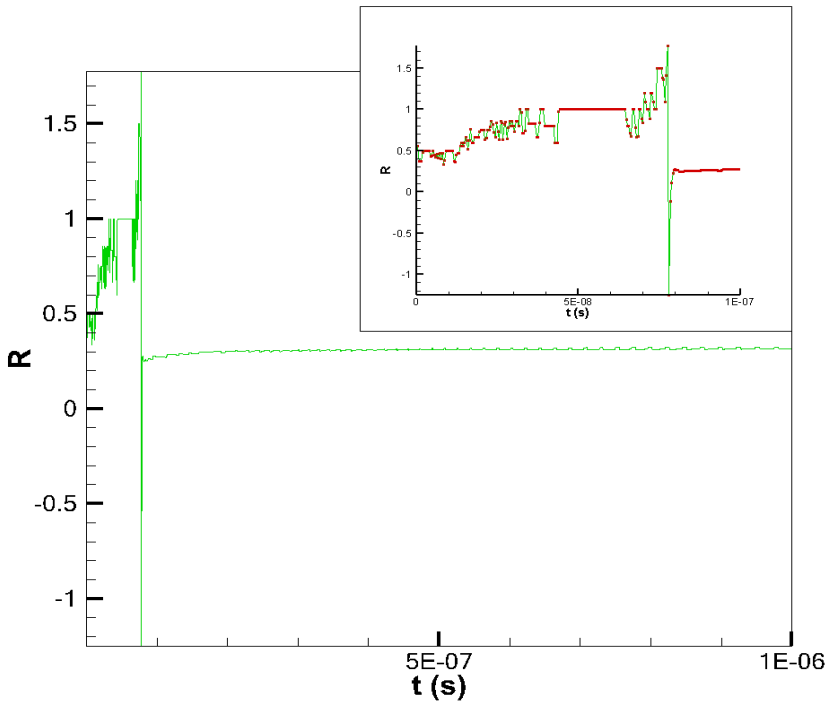

Figure 3.6 a: Plot of the convergence ratio vs time

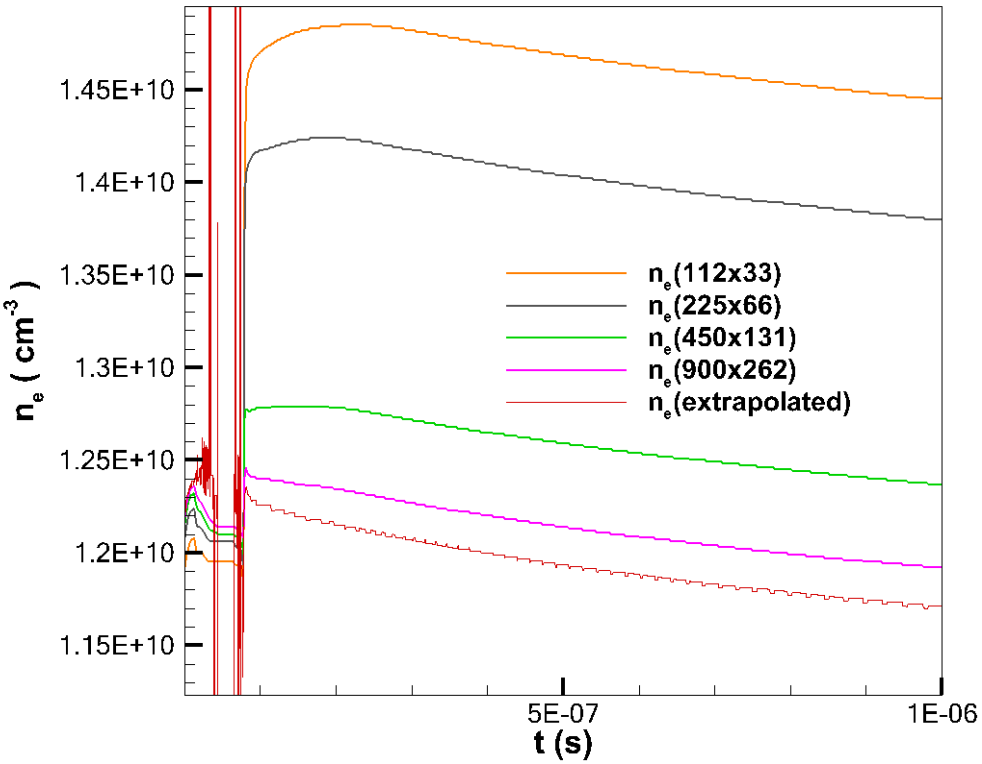

Figure 3.6b: Comparison of average electron number density at different grid resolutions and Richardson extrapolated value.

3.4 Restart and Automation

The HPEM code has a built-in restart capability. With this feature, the results on the last iteration of the simulation are written into a restart file, and this restart file is used for restarting the simulation. In restarting the simulation, we cannot alter the conditions of the simulation like the number of species, pressure, chemistry, or geometry, since these values are written into the restart file. We can, however, change the voltage applied and other parameters which control the simulation like the calculation methods.

The experimental case selected for simulation has a PRF of 30 kHz, which implies the time between two consecutive pulses is 33 μs. The length of the pulse with non-zero voltage is 0.15 μs beyond which there is no voltage applied as shown in Figure 3.7.

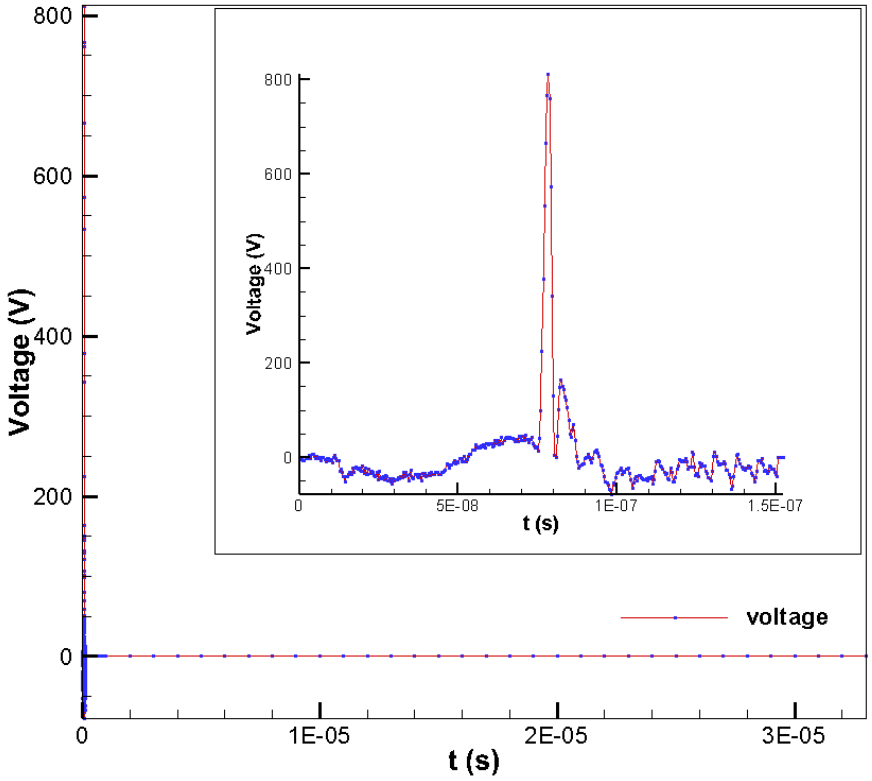

Figure 3.7: Plot of the voltage pulse input for the simulation.

To obtain better computational resolution during the pulse we chose to have atleast 10 time-steps to resolve 3 ns FWHM of the pulse, so a time step of 0.4 ns or lower had to be used for

the simulations. Since we cannot afford to use this time step for an entire pulse and decay of 33 μs, we chose to run the case with two different time steps for the simulation. A smaller time step 0.4 ns is used during the pulse up to 1 μs , and then the case is restarted with a relatively larger time step (10 -100 ns) when no voltage is applied, until 33 μs. This procedure reduced the overall computation time.

The restart case was implemented on a grid resolution of 225 x 66 (N_z x N_r), first a time step of 0.4 ns was used up to 1 μs and then a time step of 10 ns and 100 ns were employed until the beginning of the next pulse i.e 33 μs. The average electron number density and electron temperature are compared to show a relative change of less than 1% in both electron number density and average electron temperature. The comparison plots are shown in Figure 3.8.

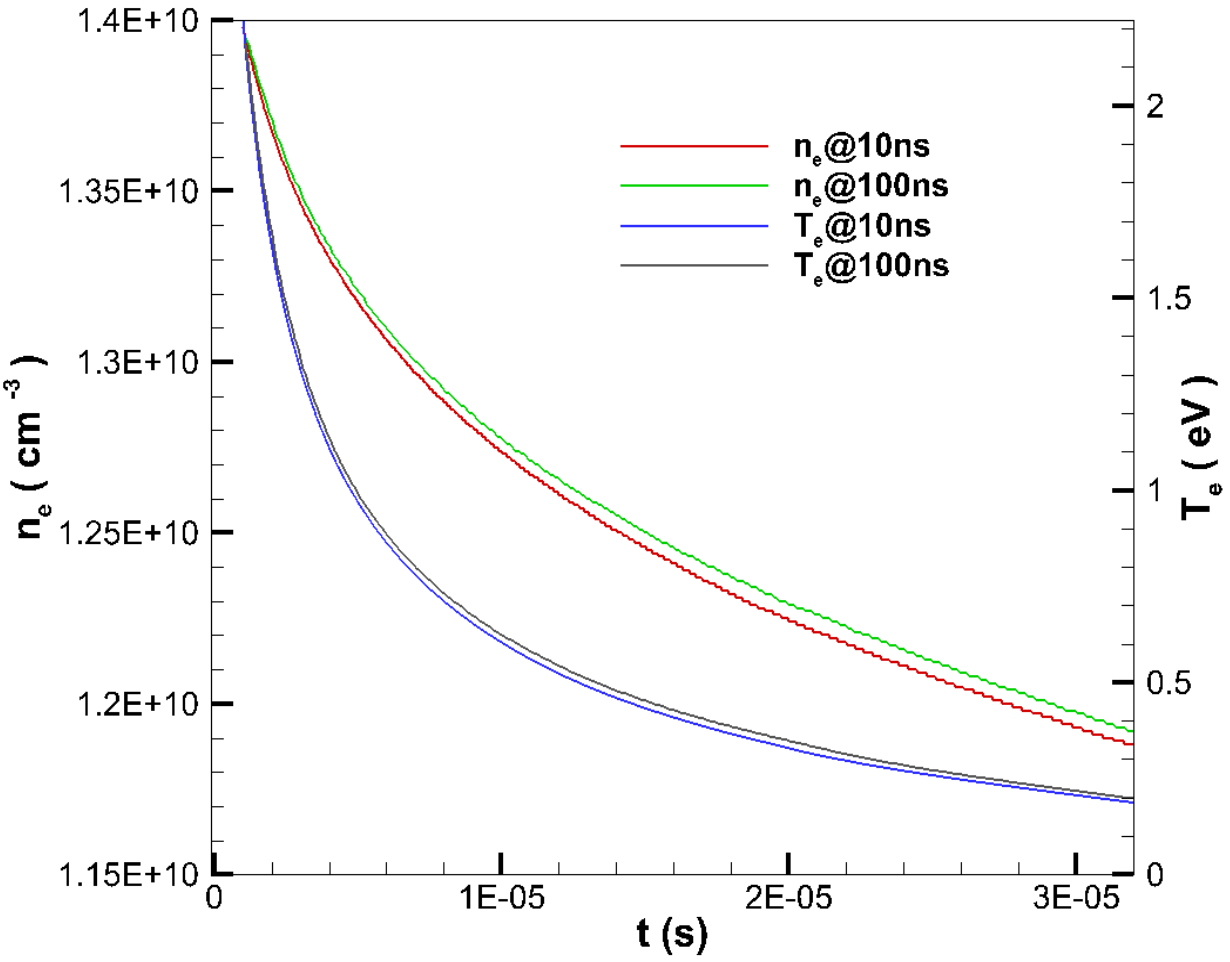

Figure 3.8: Plot of average electron number density and average electron temperature during the decay after the pulse with 10 and 100 ns time steps.

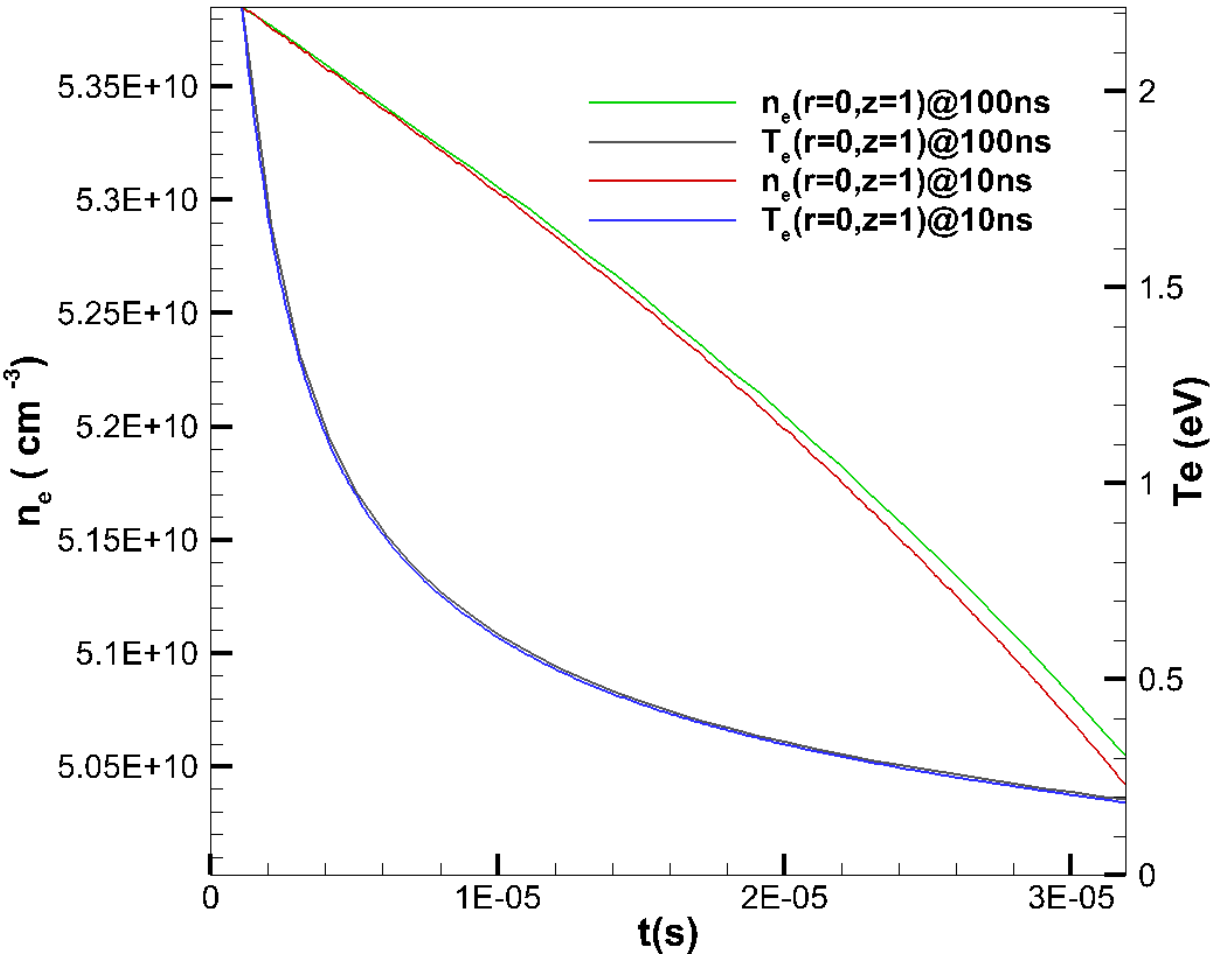

Figure 3.8b: Plot of electron number density and electron temperature at the center of the plasma domain during the decay after the pulse with 10 and 100 ns time steps.

The value of the average electron number density is known from experiments, but the initial number densities of other species in the plasma are unknown. We can assume some initial number densities for other species, but we may not be able to capture the accurate physics from the plasma experiments. Thus, we need to run the pulses until we reach a periodic state, and we need to automate this restart for many pulses. Total time to run the simulation for one pulse of 33 μs with a grid resolution of 225x66 takes around 20 hrs, so a grid resolution of 67x131 was chosen to show that the automation worked and that the periodic state could be reached after running for some pulses. The run time for each pulse was reduced to 3 hrs with this grid resolution. The initial number densities of ions have been varied for 3 different conditions and the simulation reach the same state after running for a few pulses as shown in Figure 3.9

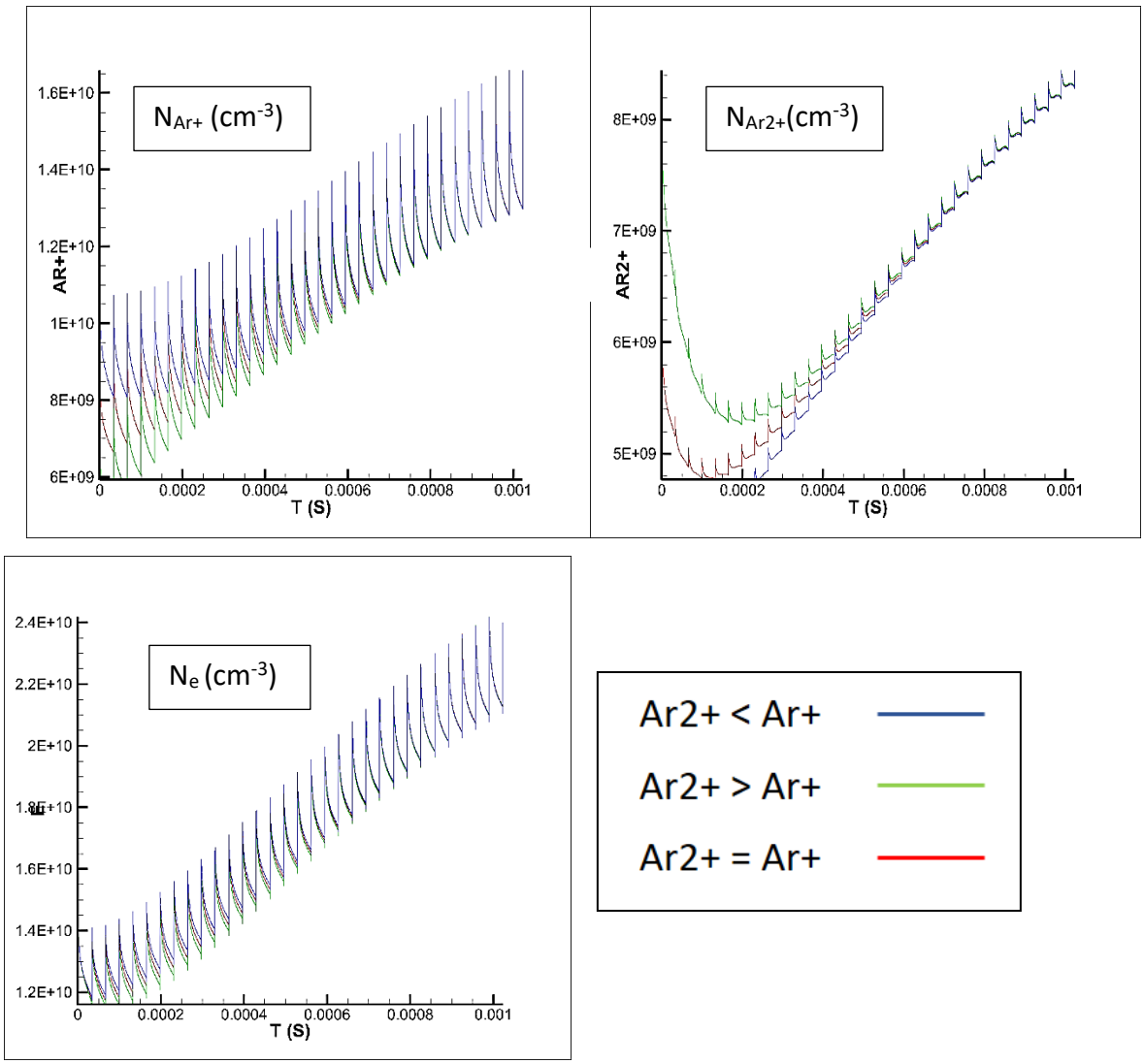

Figure 3.9: Plots of average electron and ion number densities for three different initial ion number densities.

Thus, the initial composition of plasma doesn't affect the simulation. The automated program has been run until we reached a periodic state. The results for these calculations, plots of the average number densities of electrons and ions, are shown in Figure 3.10. A single pulse was simulated for finer grid resolutions by initializing the simulation with the mole fractions of species observed during this periodic state.

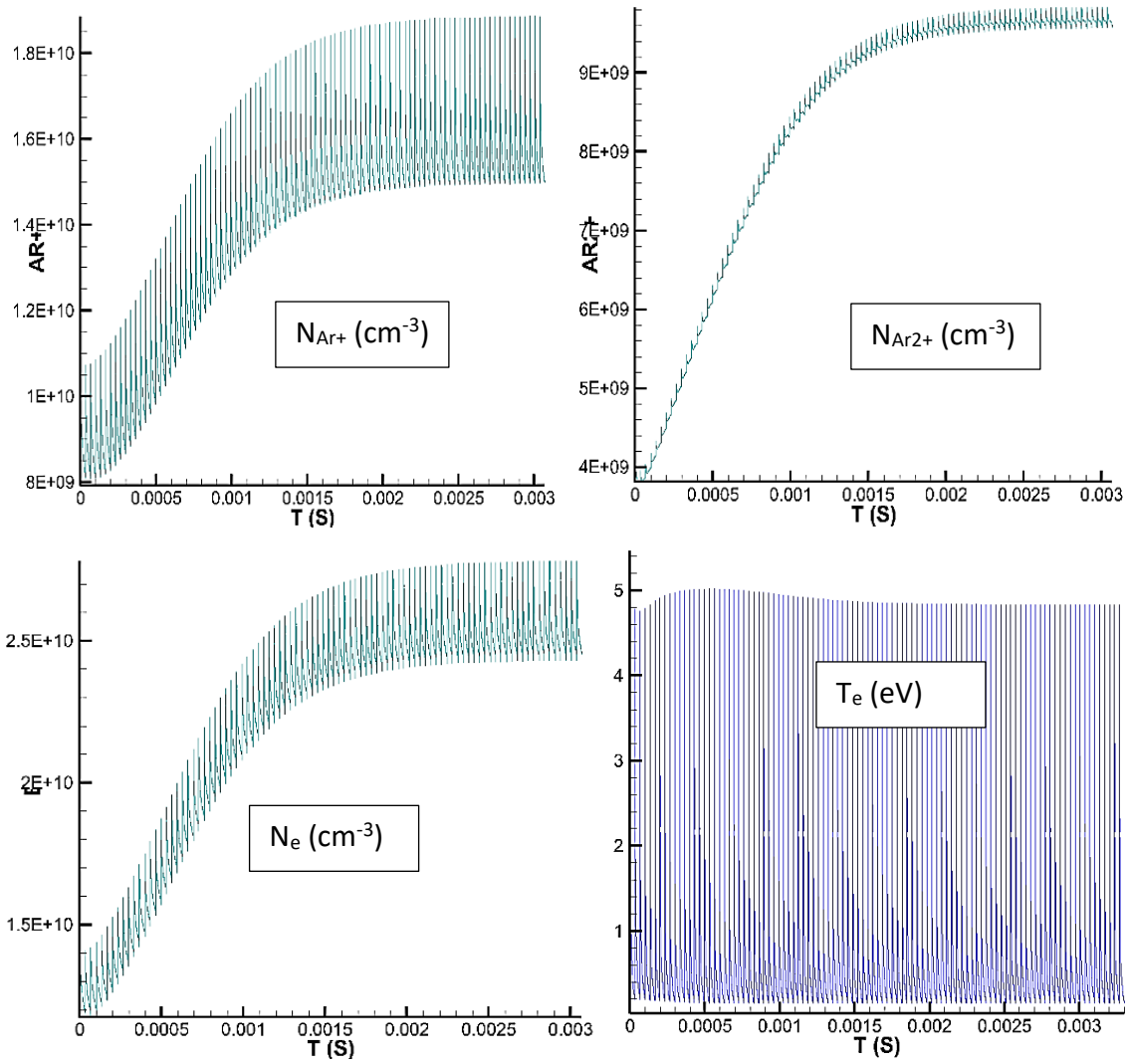

Figure 3.10:Plots of average number densities of electrons and ions and average electron temperature, with the simulation run for 100 pulses.

4. RESULTS AND DISCUSSION

The simulation was setup as discussed in Section 3.2. We wish to opt for analyzing the results for grid resolution of 225x66 (N_z x N_r) to compare with the experimental results due the ease of processing the data. The current was calculated at the cathode and anode and compared with the experimental values. Also, the average electron number density in experiment and simulation has been compared.

4.1 Current

HPEM also outputs the 2D-data at every iteration of the simulation in Tecplot format. This data file is used to compute the conduction and displacement current densities at every iteration. These current densities $\vec{j}$ are integrated to compute the respective currents *I*:

$$I = \int \vec{j}.\overrightarrow{dA} \quad \text{where } \overrightarrow{dA} = \vec{n}dA \tag{4.1}$$

Using the 2D data, a specific control volume has been chosen in the plasma domain as shown in Figure 4.1. The current densities at the grid points on the surface of the control volume are calculated and then integrated with the area normal to the current densities.

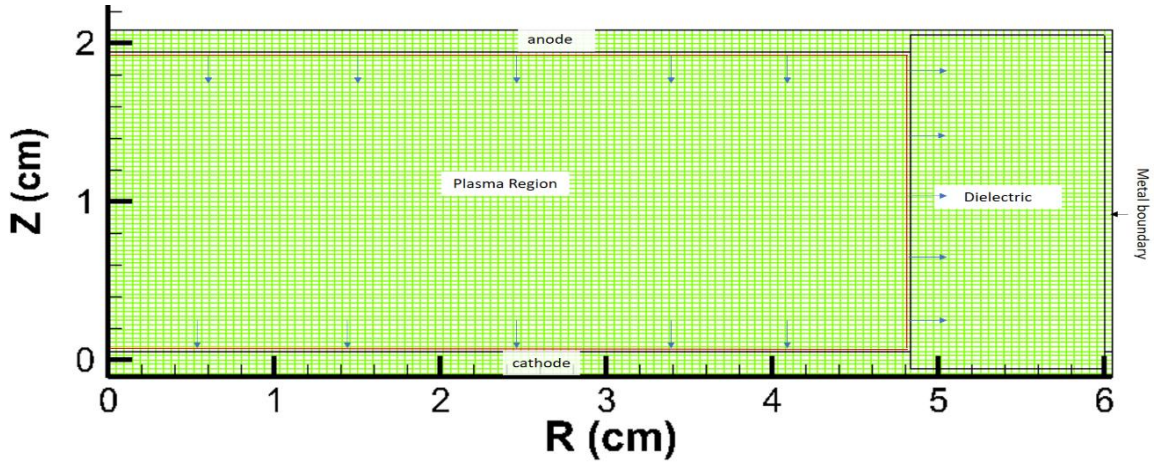

Figure 4.1: Mesh with control volume used to estimate the currents at the cathode and anode and radial currents. The red line shows the Control Volume and the Blue arrows show the flow of current.

The conduction current density is calculated from the flux of the charged species.

$$\vec{J_c} = \sum q_i \vec{\Gamma_i} \tag{4.2}$$

where Γ_i is the flux of charged species *i*, q_i is the charge on the species *i*.

The presence of time varying electric fields in the plasma implies the displacement current has a significant contribution towards the total current. The displacement current density is calculated using the derivative of local electric field.

$$\vec{J_d} = \epsilon_0 \frac{\partial \vec{E}}{\partial t} \tag{4.3}$$

The displacement current density was estimated using a second-order backward-differencing scheme in time to obtain the derivatives of electric field at that time at a given grid point. To compute the integral of the current density over a given surface, the current densities at the grid point are multiplied with the unit area of the cell, and all the values along the surface are added.

The comparison of displacement currents for the simulation run with different time steps can be used to show that the code converges in time. The simulation is convergent in time since the displacement currents observed for different time steps are converging as seen in Figure 4.2.

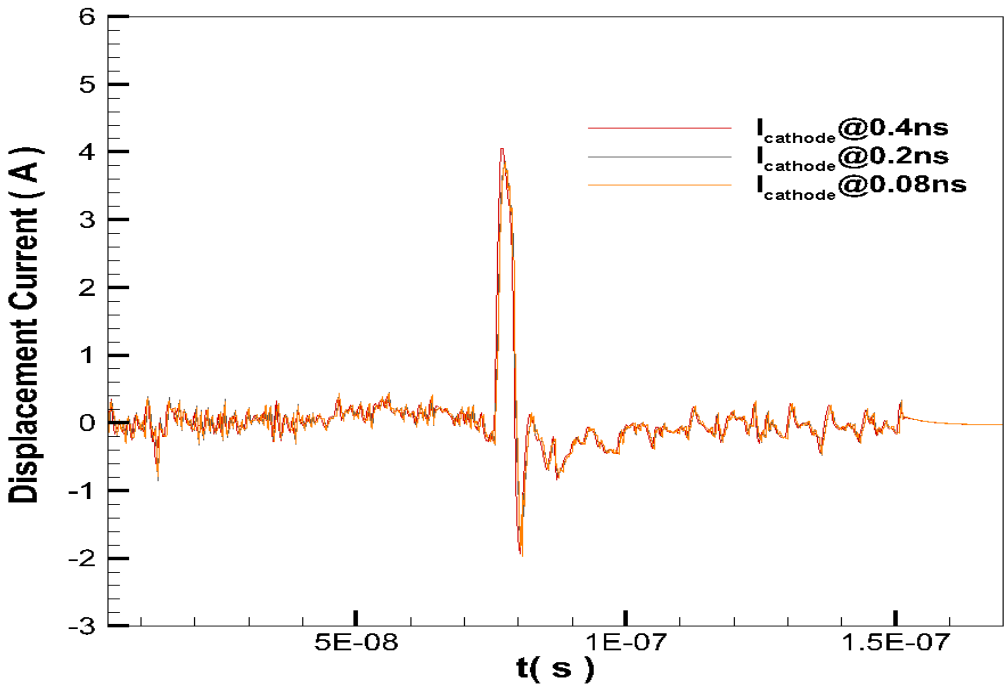

Figure 4.2: Plot of the displacement current at the cathode for different time resolutions to check for convergence in time.

The current at the cathode, anode and radial currents at the right most boundary, were computed using the control volume mentioned in the Figure 4.1. These currents are compared to the experimental values for current in Figure 4.3.

The observed plots show that the simulated current is less than the experimental value. The experimental results correspond to a discharge at a periodic state, whereas the simulation has been run for one pulse with just the information of applied voltage and the initial electron number density from microwave interferometry. The actual number densities of species to initialize the simulation had to be guessed, since the simulation with a resolution of 225x66 takes unacceptable run times when run for many pulses until steady state is reached.

The calculated current leaving the anode is not equal to the current entering the cathode, which implies a flow of current in the radial direction in the control volume previously mentioned. This motivates a check of conservation of the current in the control volume.

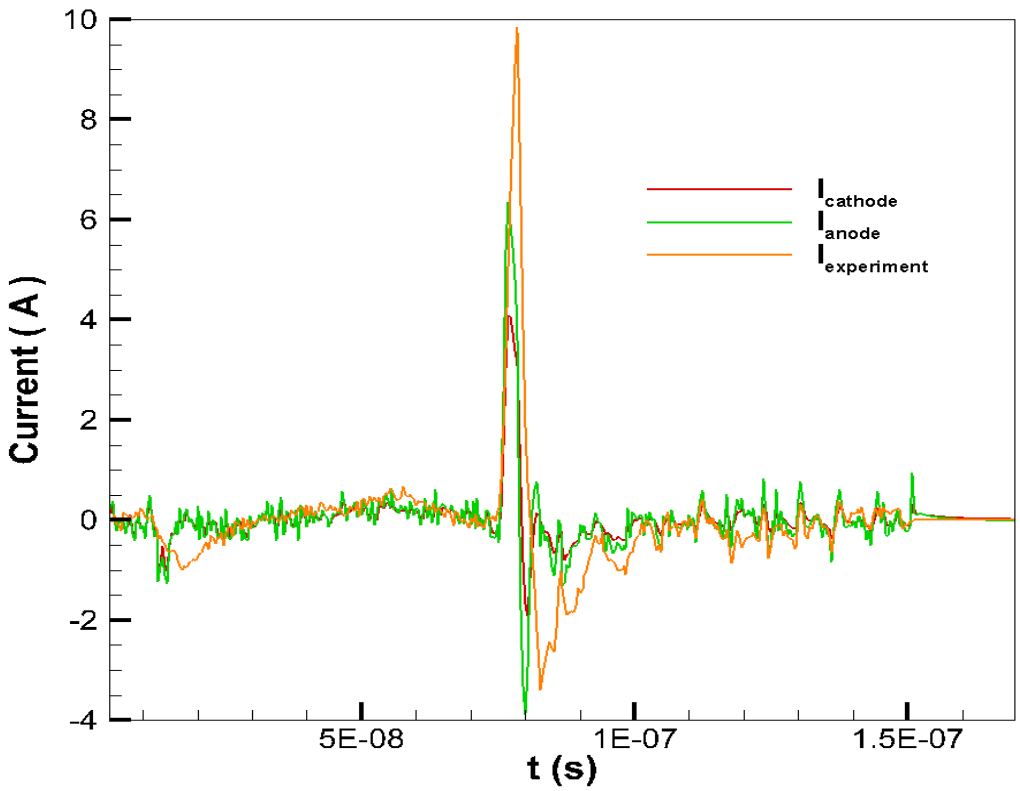

Figure 4.3: Plot of net current at the cathode and anode.

4.2 The Maxwell's Equations and Current Conservation.

Maxwell's equations, Eq 4.4, can be used to derive the current conservation equation.

$$\nabla.\vec{E} = \frac{\rho}{\epsilon_0} \;\; ; \;\; \nabla \times \vec{B} = \mu_0 \left(\vec{J}_c + \epsilon_0 \frac{\partial \vec{E}}{\partial t} \right) \;\; ; \;\; \nabla.\vec{B} = 0 \;\; ; \nabla \times \vec{E} = -\frac{\partial \vec{B}}{\partial t} \tag{4.4}$$

$$\nabla.\left(\nabla \times \vec{B}\right) = 0 = \mu_0 \nabla.\left(\vec{J}_c + \epsilon_0 \frac{\partial \vec{E}}{\partial t} \right) \tag{4.5}$$

$$\nabla.\left(\vec{J}_c + \epsilon_0 \frac{\partial \vec{E}}{\partial t} \right) = 0 = \nabla.\left(\vec{J}_c + \vec{J}_d\right) \tag{4.6a}$$

$$\nabla.\vec{J}_c + \epsilon_0 \frac{\partial (\nabla.\vec{E})}{\partial t} = \nabla.\vec{J}_c + \frac{\partial \rho}{\partial t} = 0$$

(4.6b)

By integrating Eq 4.6a in the control volume we have

$$\iiint \nabla.(\vec{j}_c + \vec{j}_d)\, dV = \oiint (\vec{j}_c + \vec{j}_d).d\vec{A} = 0$$

(4.7)

By integrating equation 4.6b in the control volume we have

$$\iiint (\nabla.\vec{j}_c + \frac{d\rho}{dt})\, dV = \oiint \vec{j}_c.d\vec{A} + \iiint \frac{\partial \rho}{\partial t}\, dV = 0$$

(4.8)

Equation 4.7 implies the net current (displacement + conduction) through the control volume should be zero. So, $I_{anode} - (I_{cathode} + I_{radial}) = 0$, this has to be checked to show that the current is being conserved during the simulation. The plot of $I_{anode} - (I_{cathode} + I_{radial})$ shows that the current is conserved for the simulation but there is a current imbalance observed near the time of the peak voltage of the pulse as seen in Figure 4.4. This could be a result of the calculation of the displacement current from the time derivative of electric field; near the peak of the pulse the electric field gradients are high.

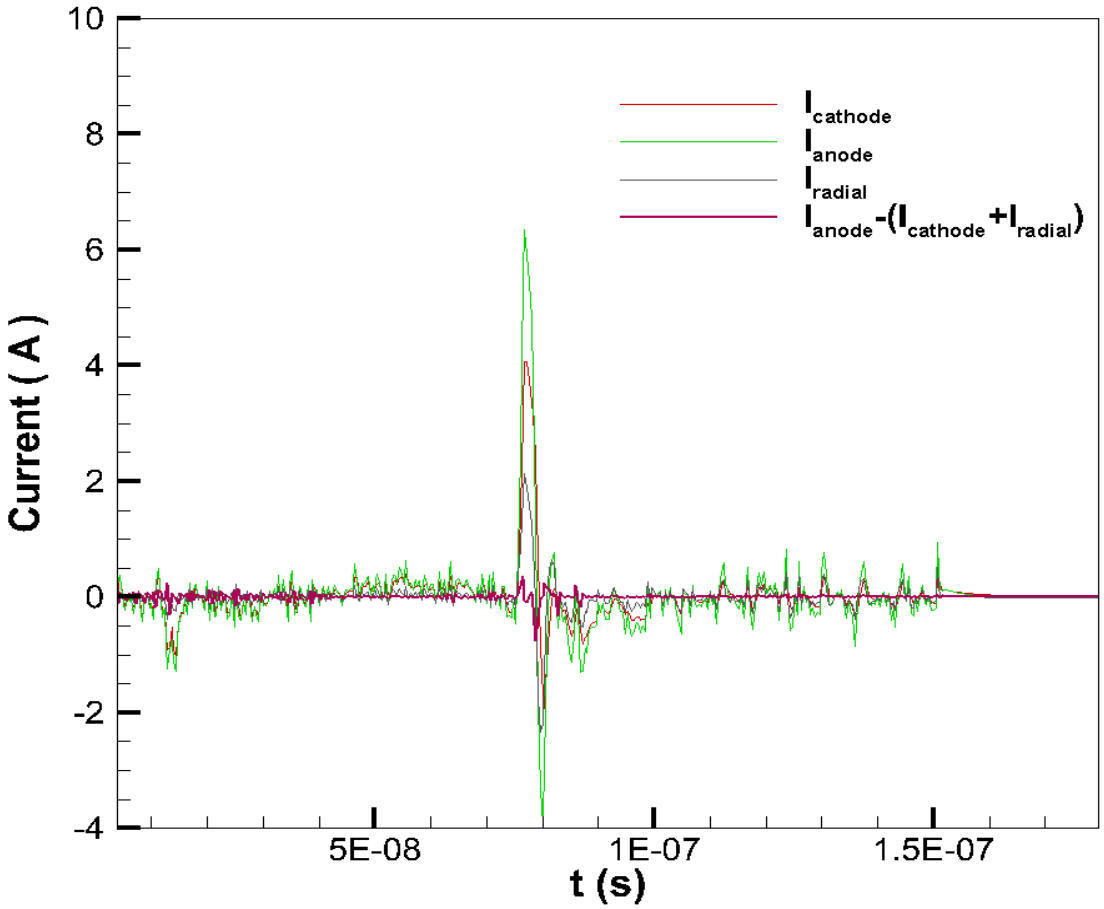

Figure 4.4: Plot of current observed and the conservation of current.

4.3 Electron and Ion Number Densities

The average electron number densities for different grid resolutions, along with the Richardson- extrapolated data, were compared with the experiments, and the results did not agree as seen in figure 4.5a. This could be due to the choice of initial number densities for the transient species. The extrapolated results for the average electron number density doesn't seem to converge during the pulse peak < 80 ns but beyond that point the results converge, this could be due to the choice of time step for the finer grid. A simple estimate shows that the courant limit is just barely satisfied for the given grid resolution of 900 points in N_z. Our attempts to decrease the time step and run the simulation were unsuccessful due to extremely unreasonable run times.

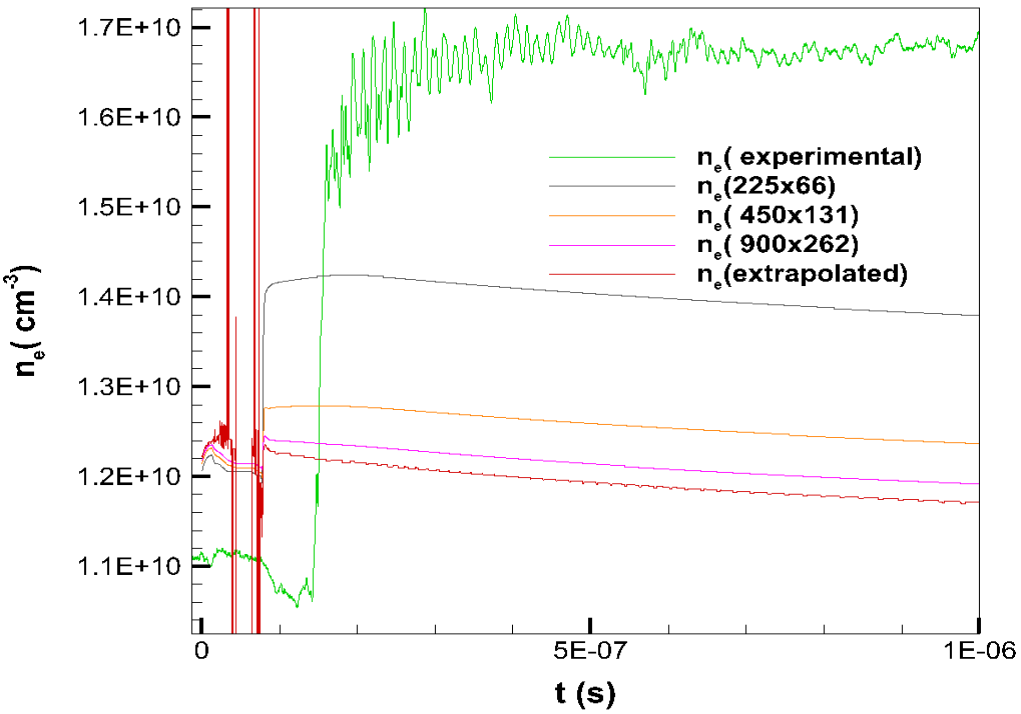

Figure 4.5a: Plot of the average electron number density

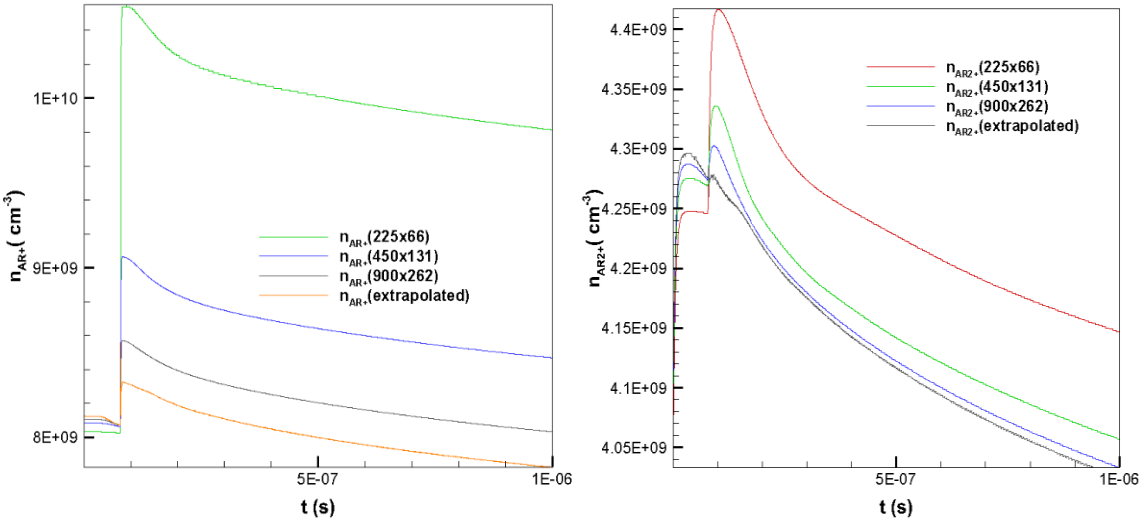

Figure 4.5b: Plot of the average ion number densities

4.4 Cathode Sheath

The formation of cathode sheath is an important phenomenon in electric discharges. The axial electric field in the cathode sheath will be high, so a profile plot of axial electric field at R=0 during the pulse peak reveals the formation of cathode sheath, as seen in Figure 4.6a.

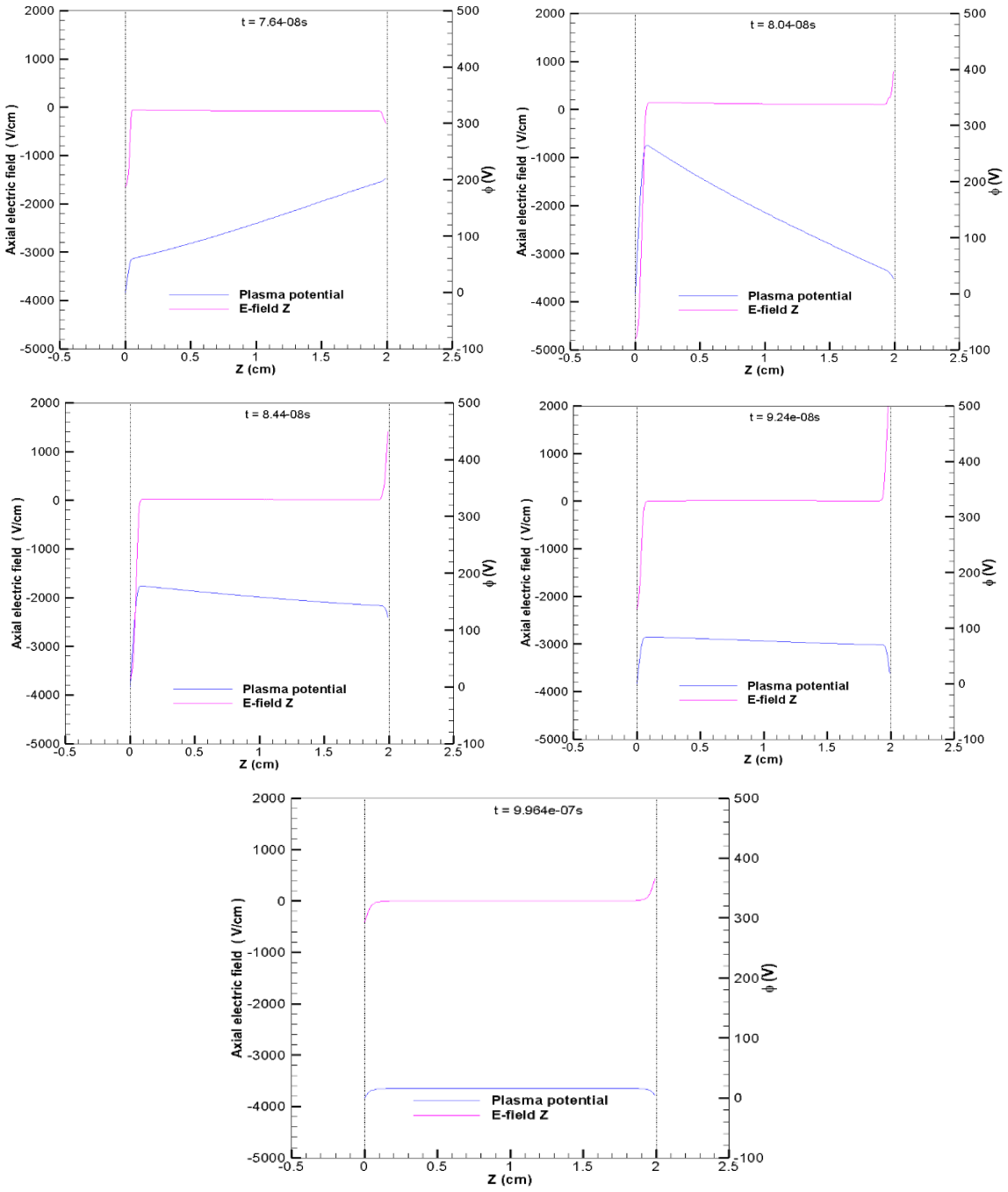

Figure 4.6 a: Profile plot of the axial electric fields and plasma potential at different times during the pulse.

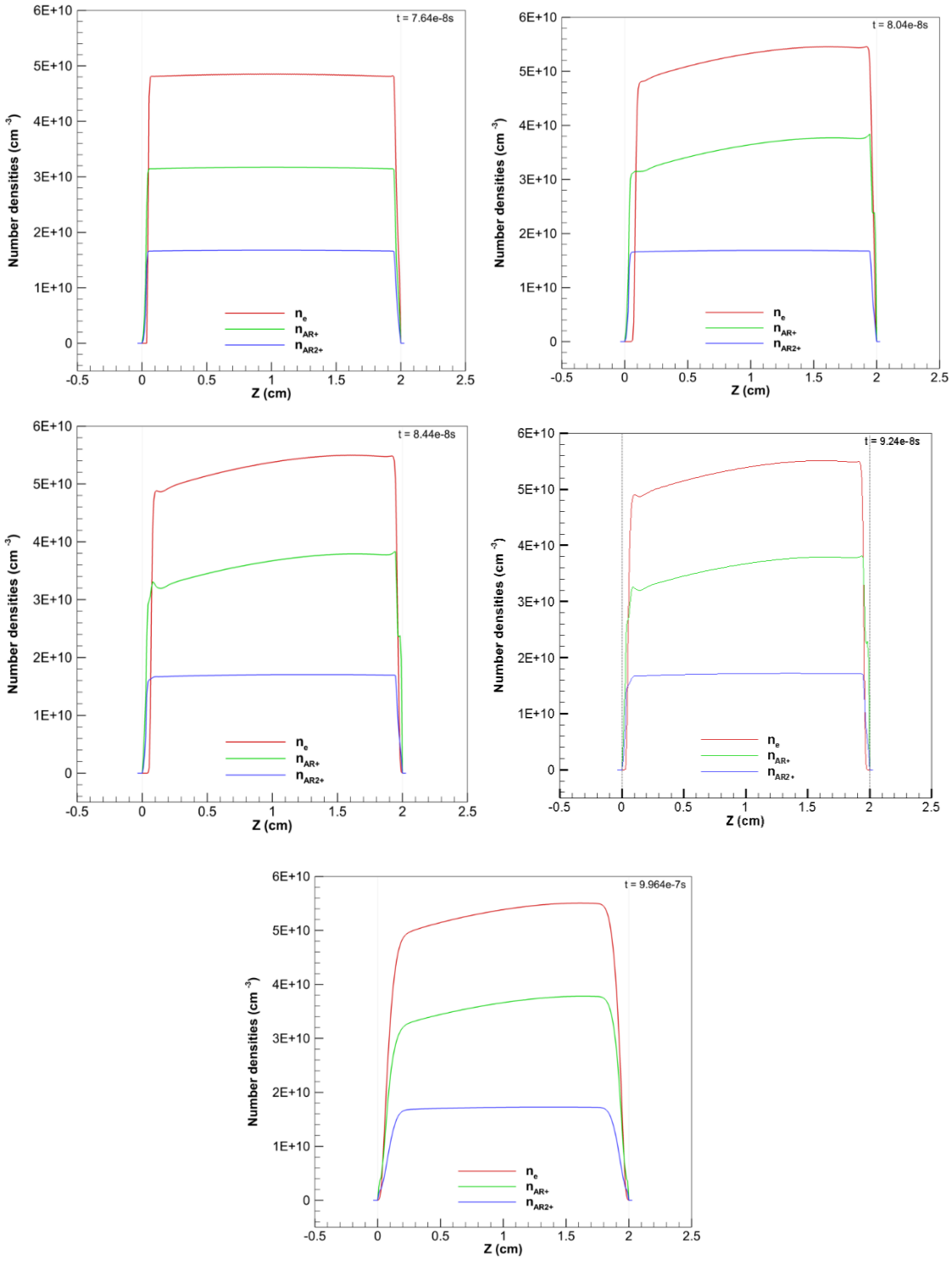

Figure 4.6b: Profile plot of the number densities of electrons and ions at different times during the pulse.

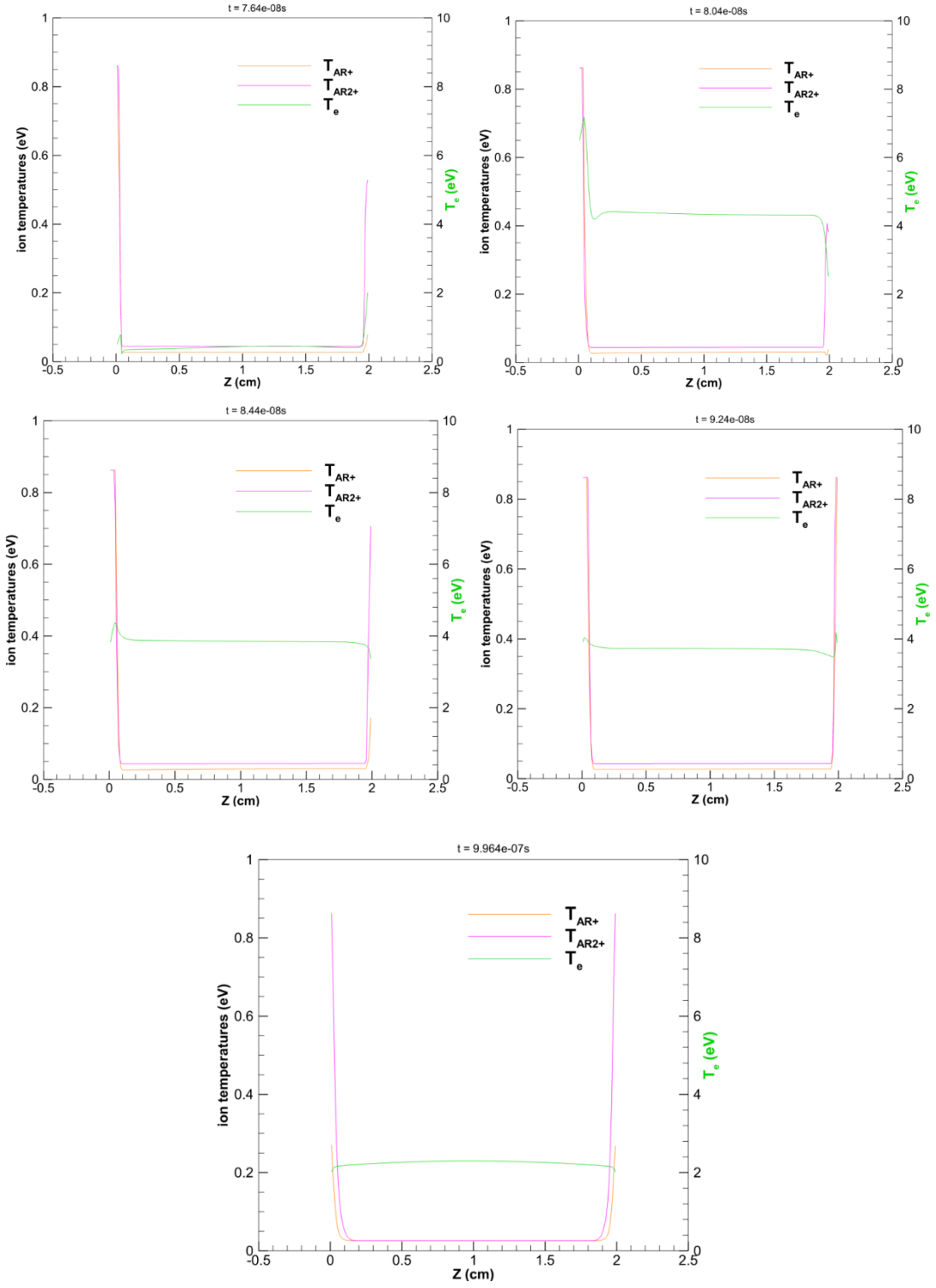

Figure 4.6c: Profile plot of the electron and ion temperatures at different times during the pulse.

4.5 Two Sheaths

During the trailing edge of the pulse, the applied voltage is zero, but the plasma still has a potential as seen in Figure 4.7b. The electrons are absorbed and lost at the electrodes relatively faster than the ions. This loss of electrons at both the electrodes causes us to observe sheath at both the electrodes. In Figure 4.7a, the profile plots of axial electric fields after the pulse peak shows the formation of two sheaths at both the electrodes.

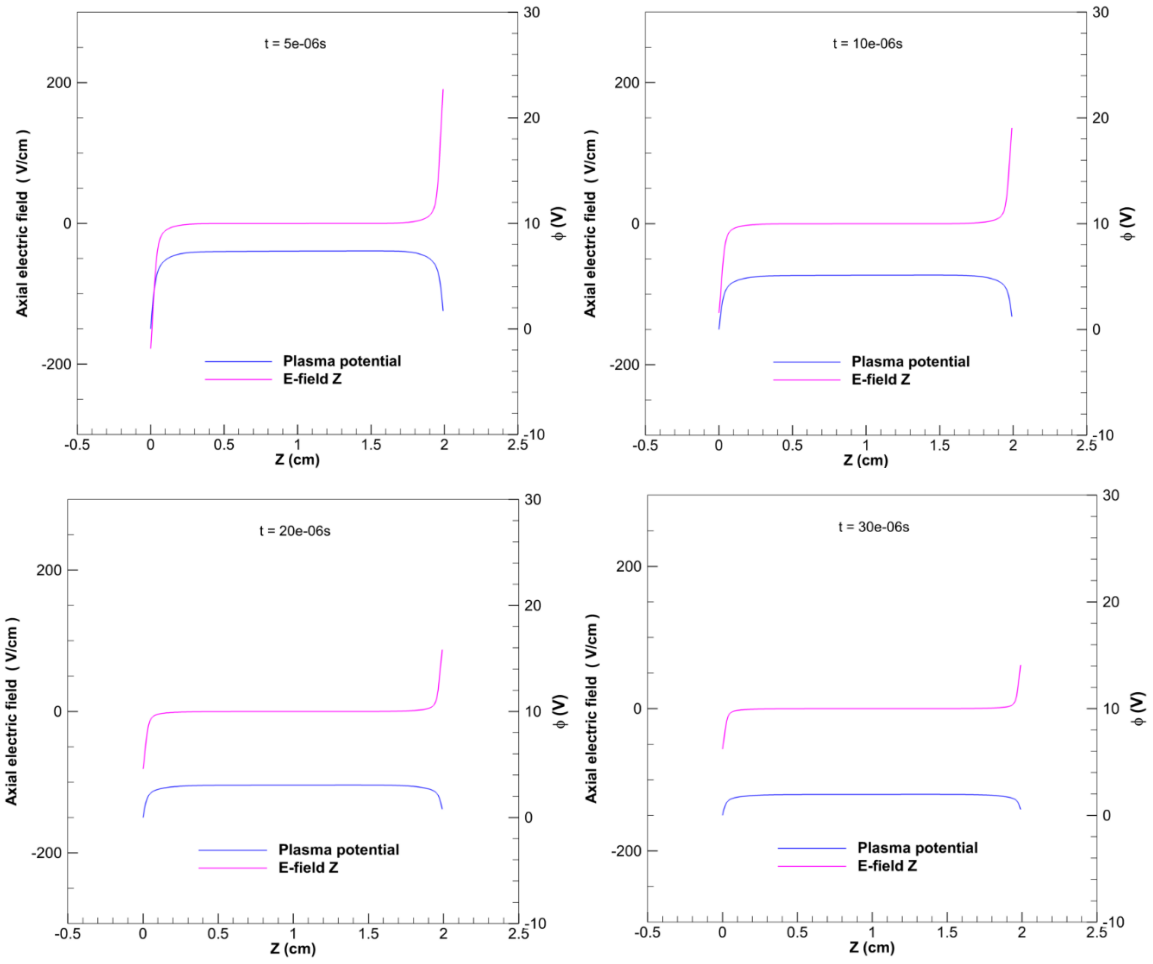

Figure 4.7 a: Profile plot of the axial electric field and plasma potential at different times during the decay part of the pulse.

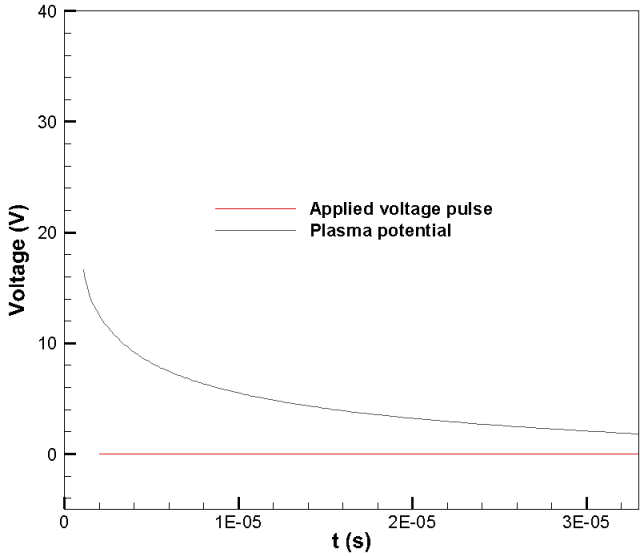

Figure 4.7b: Comparison of the plasma potential with the applied voltage during the decay part of the pulse.

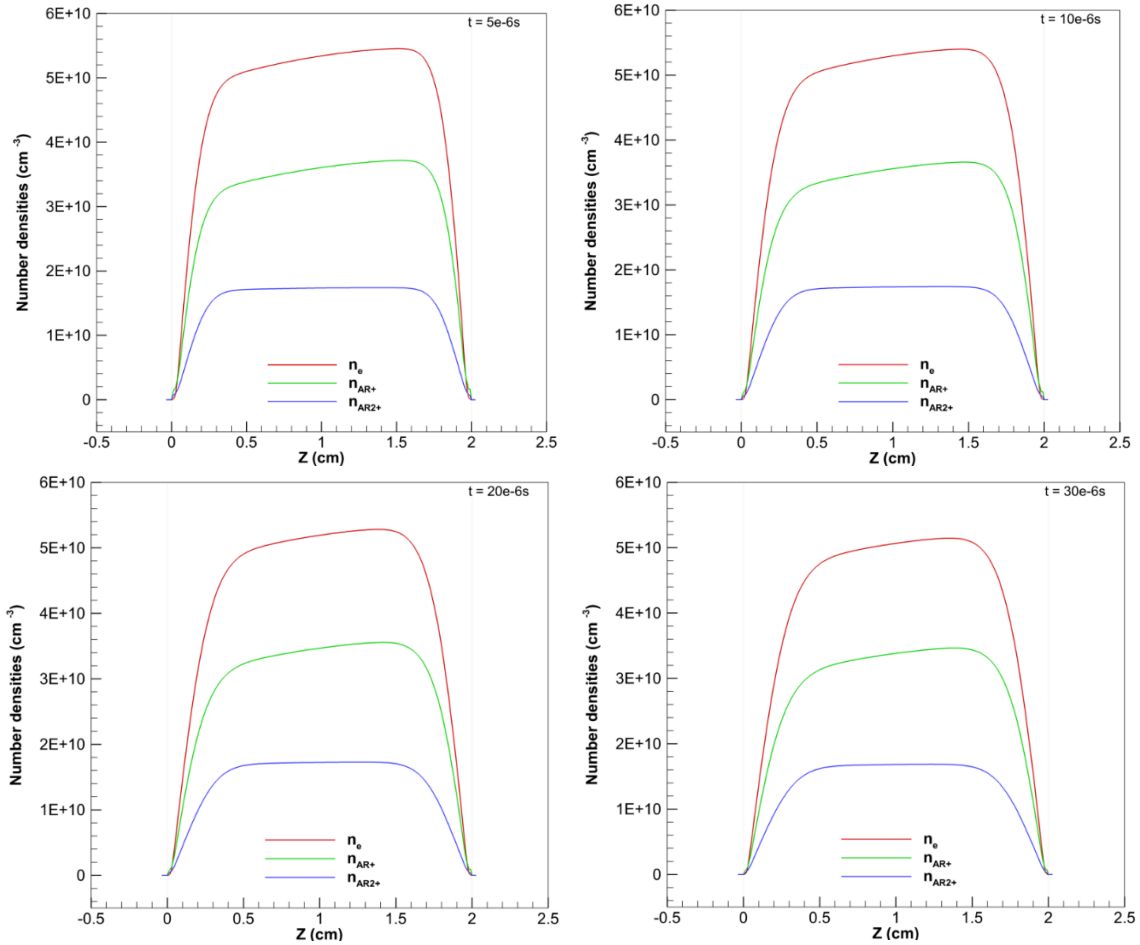

Figure 4.7c: Profile plot of the number densities at different times during the decay part of the pulse.

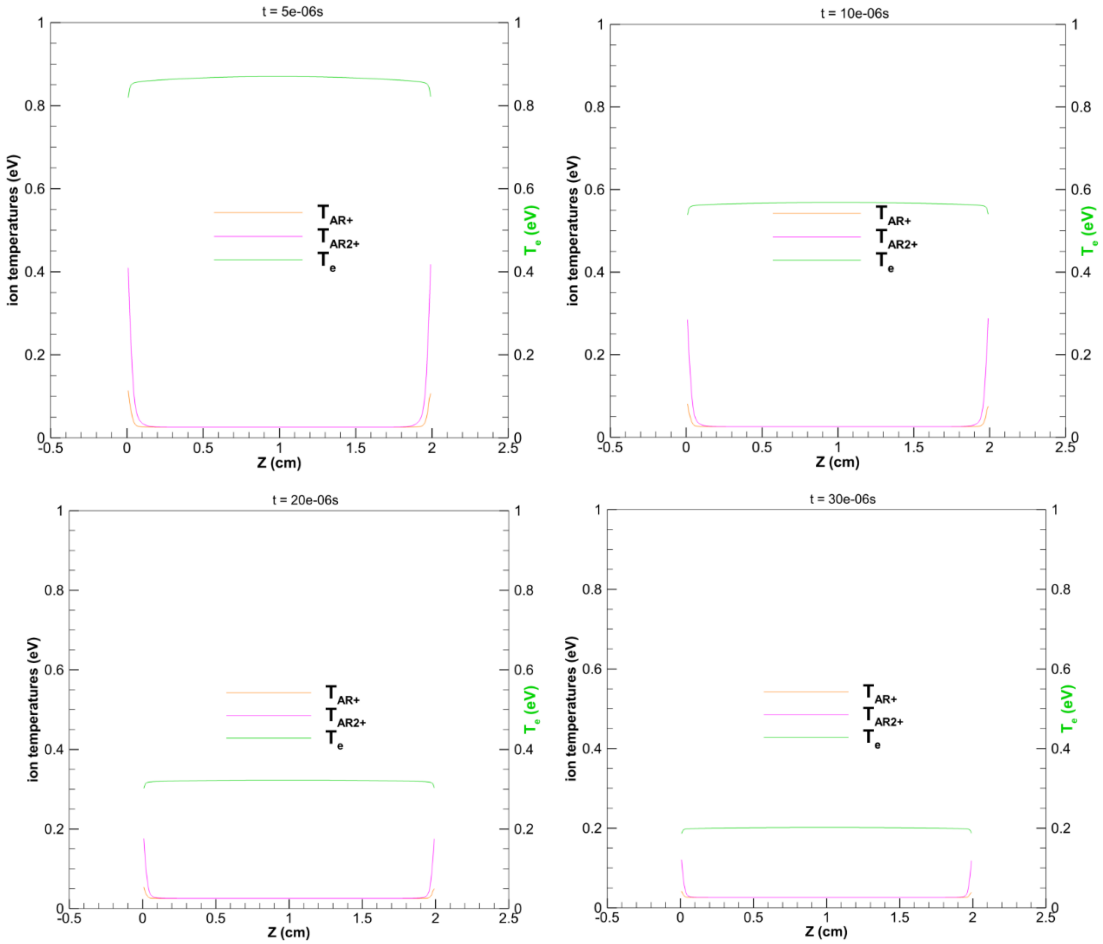

Figure 4.7d: Profile plot of the electron and ion temperatures at different times during the decay part of the pulse.

4.6 Electron Temperature and Number Density

The average electron temperature increases to a max value of 6 eV during the pulse and decreases to less than 1 eV but not to room temperature 0.026 eV, as seen from Figure 4.8a. The electron temperature decreases at a faster rate compared with the electron number density, simulated for a grid resolution of 225x66. This is promising for the development of plasma antennas. Also, the observed electron number density profile doesn't match the experimental observations as seen from Figure 4.9.

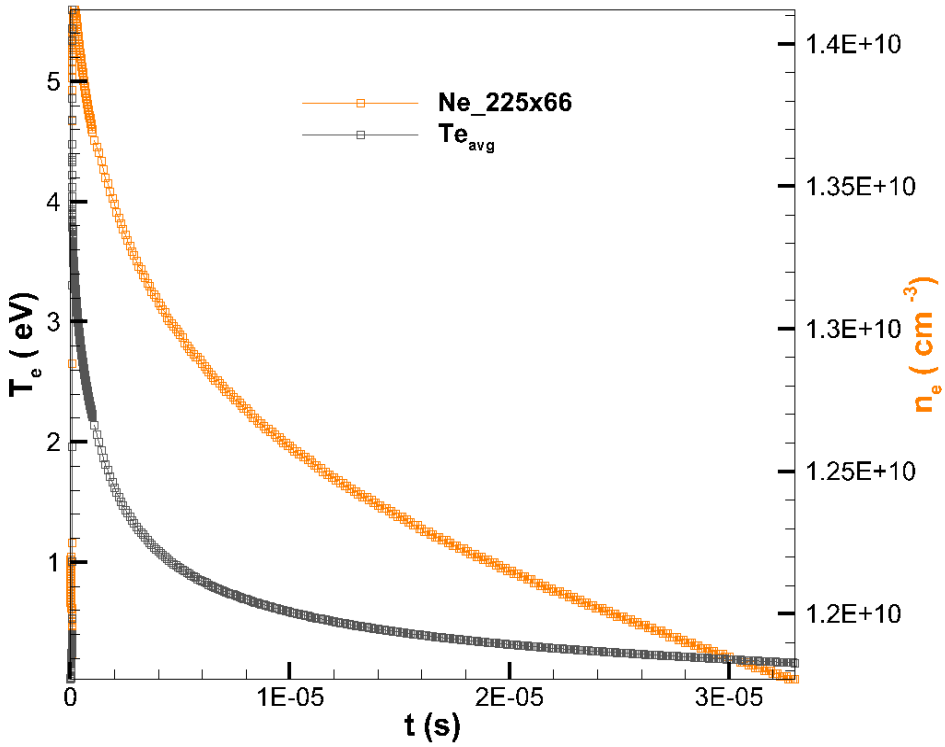

Figure 4.8 a: Plot of average electron temperature and electron number density.

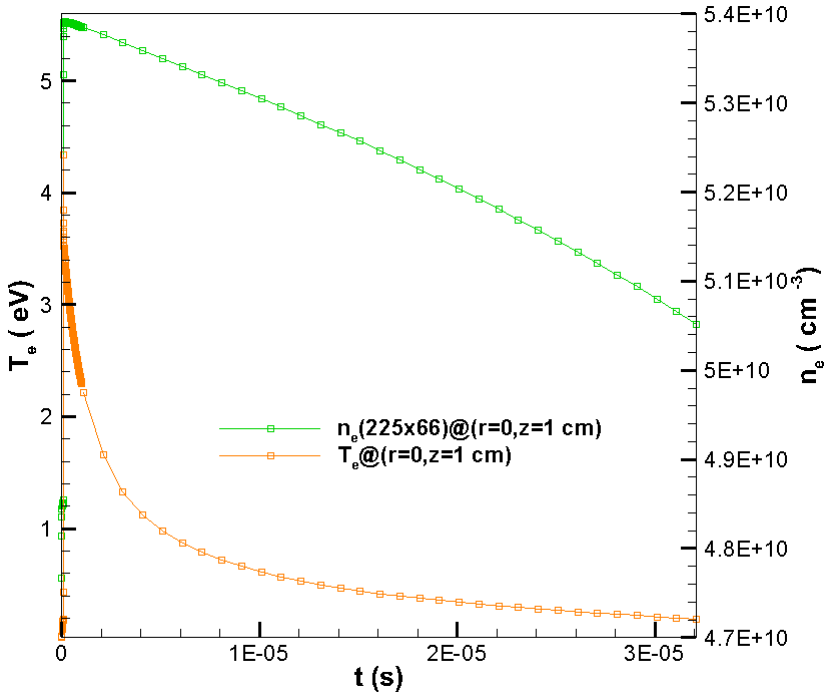

Figure 4.8b: Plot of electron temperature and electron number density at the center of the domain.

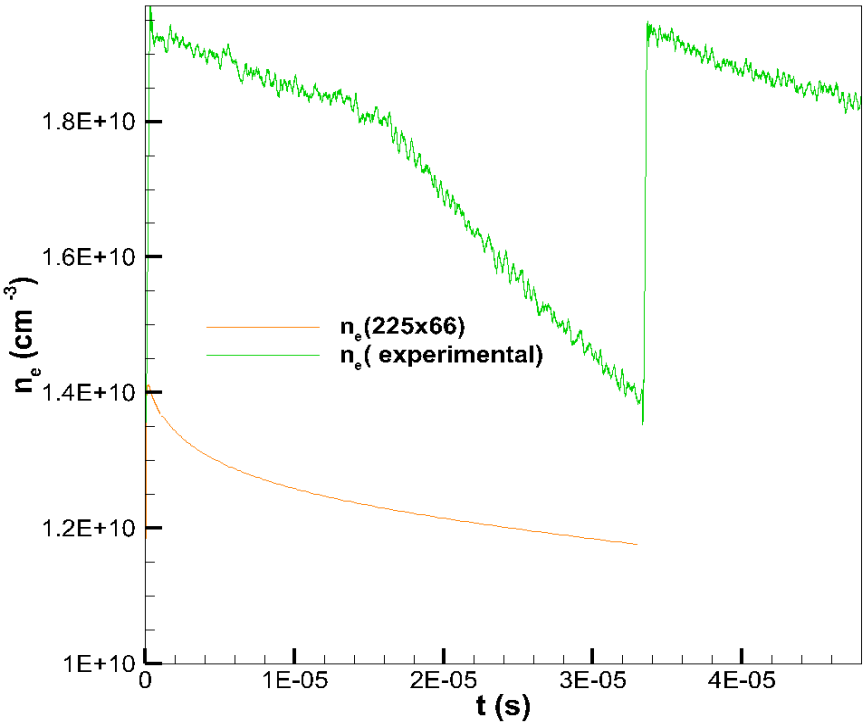

Figure 4.9: Comparison of experimental and simulated average electron number density.

4.7 Ar-H_2O Plasma

Further analysis of experimental results, Prof. Macheret has pointed out that the presence of impurities could be the cause of the decay behavior of the experimentally measured electron number density trend. The experimental team has found that presence of few ppm of water vapor in the argon gas has changed the electron number density decay behavior. So, we intend to add the minimalistic reactions involving water to the data set (Appendix B) and run the calculations for a grid resolution of N_z x N_r (225x66) with 0.045% water in argon. The average electron number densities and the average electron temperature are compared in figure 4.10a. It could be observed that the electron temperature relaxes faster to room temperature 0.026 eV with adding 0.045% H_2O to pure argon.

Figure 4.12, the decay of the electron number density shows a similar behavior compared to the experiments although the absolute values do not match ideally, including oxygen and its respective species into the reaction data set could model the experimental behavior more accurately.

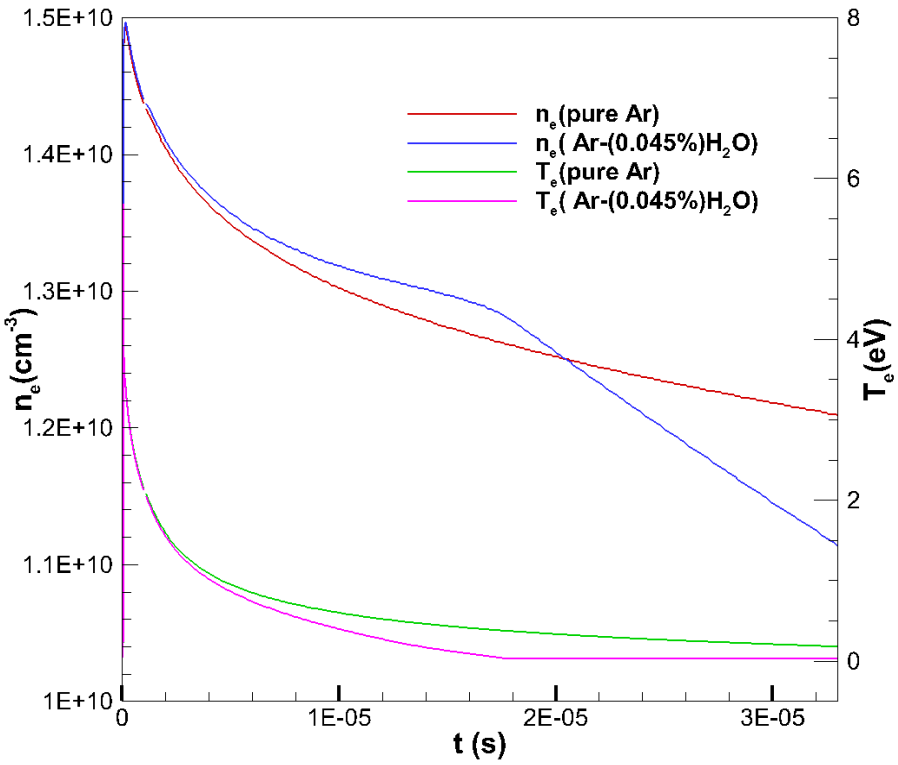

Figure 4.10 a: Comparison plot of average electron temperature and average electron number density.

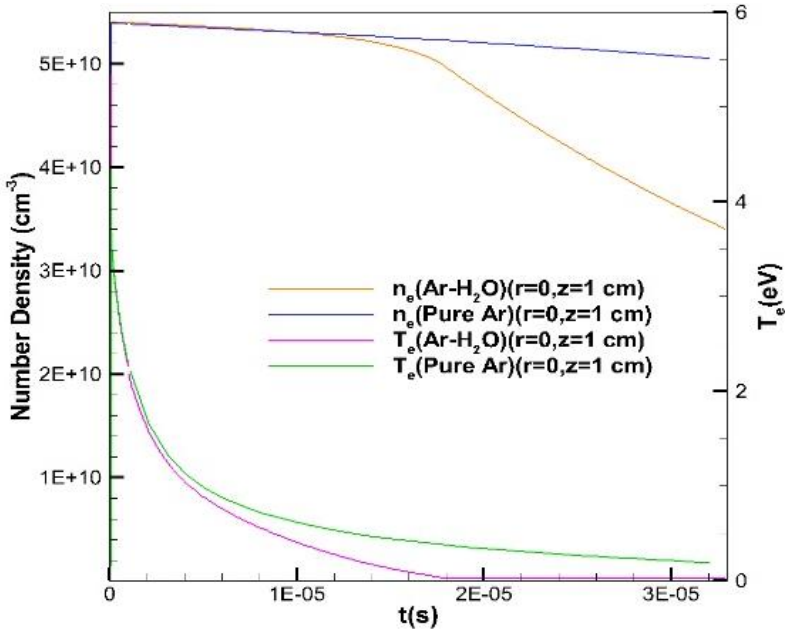

Figure 4.10b: Comparison of electron number density and temperature at the center of the domain with and without H_2O reactions.

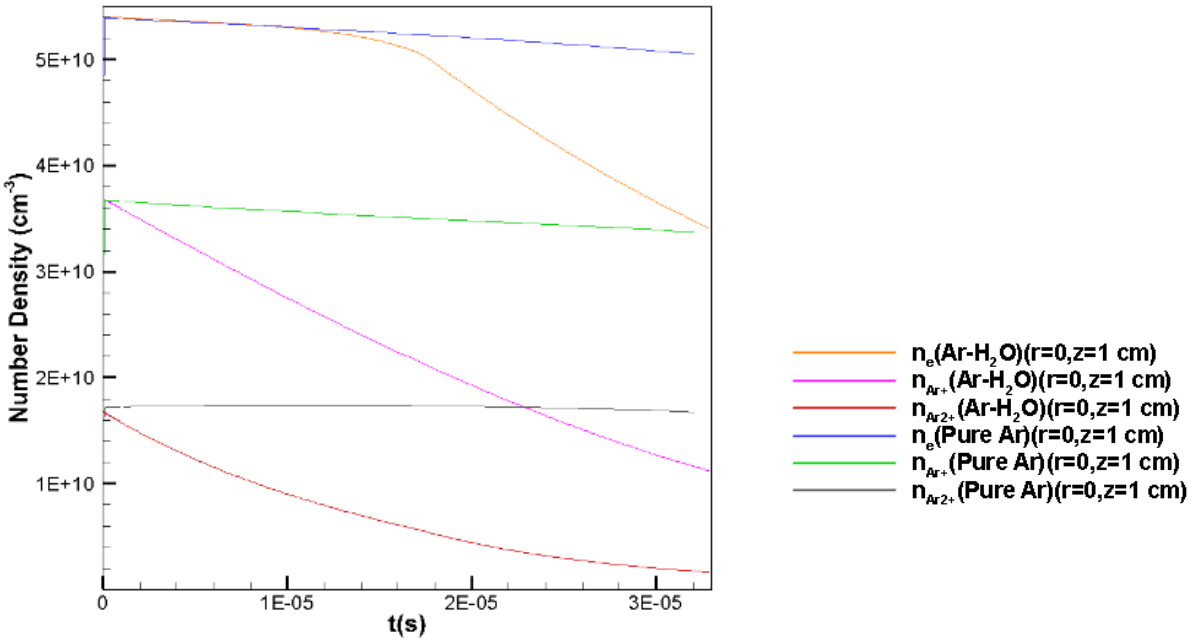

Figure 4.11: Comparison of electron and ion number density at the center of the domain with and without H_2O reactions.

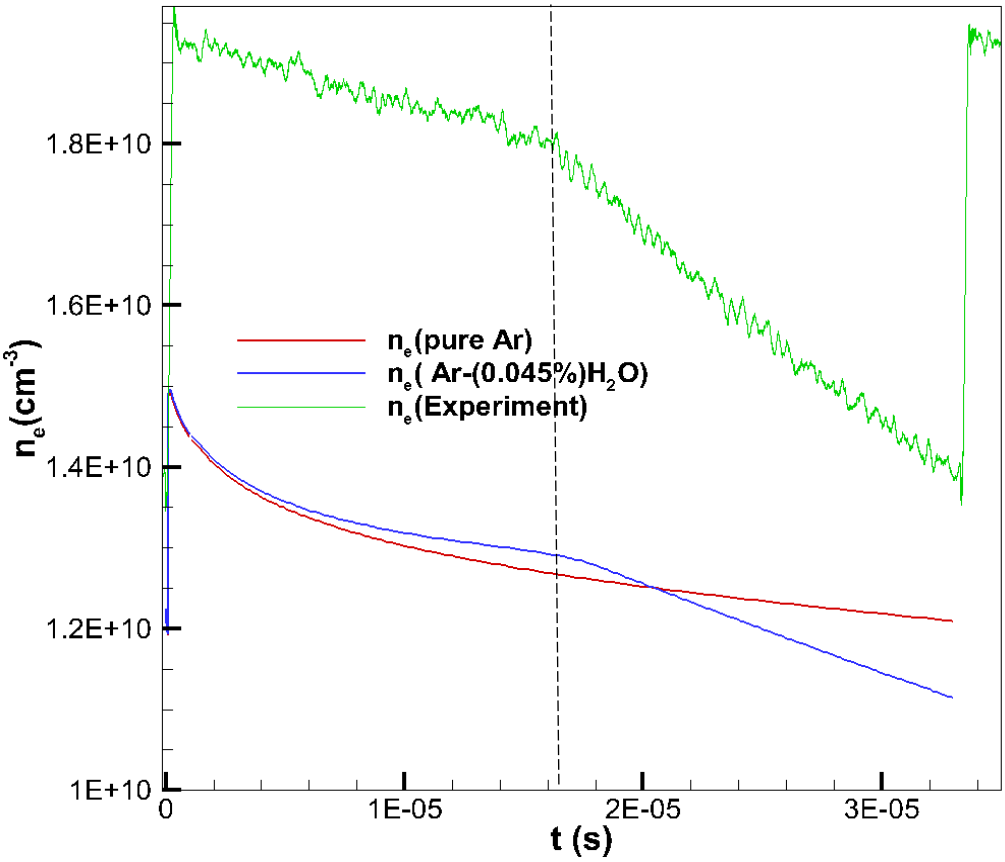

Figure 4.12: Comparison of average electron number densities with and without H_2O reactions and comparison with experiments.

5. SUMMARY AND CONCLUSIONS

The use of nanosecond pulse discharges for plasma antennas has been experimentally demonstrated at different pulse repetition frequencies. The plasma sustained at different PRF reached a periodic state, where the voltage and current were measured using the back current shunt and the average electron number density in the plasma were measured using microwave interferometry [5]. We choose to simulate a PRF of 30 kHz and compared the results to the experimental measurements. The initial composition of plasma is unknown, except for the average electron number density, and the applied voltage is available. The initial number densities of other species are input as an estimate. The simulation was run for a sufficient number of pulses to successfully show the periodic state was reached after a certain number of pulses, irrespective of the initial number densities input into the simulation. The code compromises in grid resolution were necessary to complete the simulations.

The HPEM code allowed a maximum grid resolution of 900x262 (N_z x N_r), we observed temporal convergence of the code but not spatial convergence. We made use of Richardson extrapolation to estimate the converged value; this has been demonstrated for the average electron number density calculations. The currents were calculated from the 2D data. We made a comparison with the experimental values for a grid resolution of 225x66, since the processing of 2D Tecplot data files for other resolutions (450x131,900x262) was difficult due to the massive file size; it took unacceptable loading times and processing times. The current was observed to be conserved except for a minor imbalance near the time of peak voltage. This could be due to truncation errors while calculating the time derivative of electric field during the pulse peak when the gradients of electric fields are very high.

We observed some important properties of the plasma. The cathode sheath was observed from the profile plot of axial electric field and plasma potential along the center of plasma domain. The formation of a double cathode during the plasma decay was also observed. Finally, the plots of electron temperatures reveal that the electron temperature decays faster than the electron number density during the decay phase after the pulse. This is very promising for the reduction of Johnson-Nyquist thermal noise and improvement of the antenna performance of the plasma.

A simple 0-D computational analysis of experimental results by Vladlen Podolsky and Prof. Macheret with addition of 0.045 % H_2O to the pure argon, has shown to match the experimentally observed electron number density. The experimentally observed number density shows two different rates of electron number density decay. We observe a similar behavior in the average electron number density with the inclusion of 0.045% H_2O for our pure argon simulation. The results could be made more accurate by including the electron impact reactions for oxygen species and controlling the number of electron impact reactions as per user specification.

For future work, we could use completely Monte Carlo electrons for the beam type electrons and the bulk electrons. The reaction data set with water could be improved and the plasma chemistry could also be addressed with Monte Carlo methods to improve the calculations. The simulations were run in series on a cluster, a better way to improve the computational speed would be to implement the HPEM code to run on parallel processors.

REFERENCES

[1] Mark J. Kushner, “Hybrid modeling of low temperature plasmas for fundamental investigations and equipment design”, 2009 *J. Phys. D: Appl. Phys.* **42** 194013

[2] Peter L. G. Ventzek, Robert J. Hoekstra, and Mark J. Kushner, “Two-dimensional modeling of high plasma density inductively coupled sources for materials processing”, 1994 *J. Vac. Sci. Technol. B* **12(1***)* 461-477

[3] G J M Hagelaar and L C Pitchford, “Solving the Boltzmann equation to obtain electron transport coefficients and rate coefficients for fluid models”, 2005 *Plasma Sources Sci. Technol.* **14** 722

[4] Sang-Heon Song and Mark J. Kushner, “Control of electron energy distributions and plasma characteristics of dual frequency, pulsed capacitively coupled plasmas sustained in Ar and Ar/CF4/O2”, 2012 *Plasma Sources Sci. Technol.* **21** 055028

[5] Vladlen Podolsky, Andrei Khomenko, and Sergey Macheret, “Time-Resolved Measurements of Electron Number Density in Argon and Nitrogen Plasmas Sustained by High-Voltage, High Repetition Rate, Nanosecond Pulses”, (submitted)2018 *Plasms Sources Sci. Technol*

[6] J van Dijk, G M W Kroesen and A Bogaerts, “Plasma modeling and numerical simulation”, 2009 *J. Phys. D: Appl. Phys.* **42** 190301

[7] Abbas Semnani, Dimitrios Peroulis and Sergey O. Macheret, “Plasma-enabled Tuning of resonant RF circuit”, *IEEE Transactions on Plasma Science, vol.* **44**, no. 8, August 2016.

[8] Yuri. P. Raizer, *Gas Discharge Physics*. Springer Berlin Heidelberg, 2011 (google scholar).

[9] “The 2017 Plasma Roadmap: Low temperature plasma science and technology”, 2017 *J.Phys. D: Appl. Phys.* **50** 323001

[10] Lee C G N, Kanarik K J and Gottscho R A, “The grand challenges of plasma etching: a manufacturing perspective”, 2014 *J. Phys. D: Appl. Phys.* **47** 273001

[11] Von Woedtke Th, Metelmann H-R and Weltmann K-D, “Clinical Plasma Medicine: State and Perspectives of *in Vivo* Application of Cold Atmospheric Plasma”, 2014 *Cont. Plasma Phys.* **54** 104

[12] Agarwal P and Girshick S L, “Numerical Modeling of an RF Argon–Silane Plasma with Dust Particle Nucleation and Growth”, 2014 *Plasma Chem. Plasma Proc.* **34** 489

[13] Chen Q, Li J and Li Y, “A review of plasma–liquid interactions for nanomaterial synthesis”, 2015 *J. Phys. D: Appl. Phys.* **48** 424005

[14] Mark J. Kushner, “Modeling of magnetically enhanced capacitively coupled plasma sources: Ar discharges”, 2003 *J. Appl. Phys.* **94** 1436

[15] Rajesh Dorai, Mark J. Kushner, “A model for plasma modification of polypropylene using atmospheric pressure discharges”, 2003 *J. Phys. D: Appl. Phys.* **36** 666

[16] N. A. Dyatko, Y. Z. Ionikh, I. V. Kochetov, D. L. Marinov, A. V. Meshchanov, A. P. Napartovich, F. B. Petrov, and S. A. Starostin, “Experimental and Theoretical Study of The Transition Between Diffuse and Contracted Forms of The Glow Discharge In Argon”, 2008 *J. Phys. D: Appl. Phys.*, **41** 055204.

[17] A. Bogaerts and R. Gijbels, “Role of Ar2+ Ar+2 ions in a direct current Argon glow discharge: a numerical description”, 1999 *J. Appl. Phys.* **86** 4124.

[18] J. D. C. Jones, D. G. Lister, and N. D. Twiddy, \The temperature dependence of the three-body reaction rate coefficient for some rare-gas atomic ion-atom reactions in the range 100-300 k", 1980. *J. Phys. B: At. Mol. Phys.* **13** 3247

[19] R. Johnsen, A. Chen, and M. A. Biondi,” Three-body association reactions of He+, Ne+, and Ar+ ions in their parent gases from 78 to 300 k”, 1980 *J. Chem. Phys*. **73**, 1717.

[20] S. Rauf and M. Kushner, “Argon metastable densities in radio frequency Ar, Ar/O2 and Ar/CF4 electrical discharges”, 1975 *J. Appl. Phys.*, **82**, 2805.

[21] Yukikazu Itikawa and Nigel Mason, “Cross Sections for Electron Collisions with Water Molecules”, 2005 *J. Phys. Chem. Ref. Data*, **34**, 1.

[22] Chun Fai Chan, “Reaction Cross Sections and Rate Coefficients Related to the Production of Positive Ions”, Feb. 1983, *Lawrence Berkley Lab* LBID-632.

[23] H.Tawara, Y. Itikawa, H. Nishimura, and M. Yoshino, “Cross Sections and related data for Electron Collisions with Hydrogen Molecules and Molecular Ions”, 1990 *J. Phys. Chem. Ref. Data*, **19**, 617

[24] S. O. Macheret, M. N. Shneider, and R. C. Murray, “Ionization in strong electricfields and dynamics of nanosecond-pulse plasmas”, 2006 *Physics of Plasmas*, **13**, 023502.

[25] White R D, Robson R E, Dujko S, Nicoletopoulos P and Li B, “Recent advances in the application of Boltzmann equation and fluid equation methods to charged particle transport in non-equilibrium plasmas”, *J. Phys. D: Appl.Phys.* **42** 194001.

[26] J.-P. Boeuf, “A two-dimensional model of dc glow discharges”, 1988 *J. Appl. Phys.* **63** 1342.

[27] J Poggie, I Adamovich, N Bisek, M Nishihara, “Numerical simulation of nanosecond-pulse electric discharges”, 2013 *Plasms Sources Sci. Technol* **22** 015001.

[28] Belenguer Ph and Boeuf J P, “Transition between different regimes of rf glow discharges”, 1990 *Phys. Rev. A* **41** 4447–59.

[29] Bogaerts A, Bultinck E, Kolev I, Schwaederl´e L, van Aekan K, Buyle G and Depla D, “Computer modeling of magnetron discharges”, 2009 *J. Phys. D: Appl. Phys.* **42** 194–18

[30] Hagelaar G J M, Makasheva K, Garrigues L and Boeuf J-P, “Modelling of a dipolar microwave plasma sustained by electron cyclotron resonance”, 2009 *J. Phys. D: Appl. Phys.* **42** 194019

[31] Roache P J, “Verification and Validation in Computational Science and Engineering”, 1998 (Albuquerque, NM: Hermosa Publishers)

APPENDIX A. LIST OF ARGON REACTIONS

Argon reactions used in the simulation are listed below. [16] [17] [18] [19] [20]

Table A.1: Electron impact reactions

Reactions	Reaction rate
$e + Ar(3s) \rightarrow Ar(i) + e$ Where $i = 1s_2, 1s_3, 1s_4, 1s_5$	b
$e + Ar(3s) \rightarrow Ar(4p) + e$	b
$e + Ar(3s) \rightarrow Ar(4d) + e$	b
$e + Ar(i) \rightarrow Ar(j) + e$ Where $i, j = 1s_2, 1s_3, 1s_4, 1s_5 \;\; i \neq j$	b
$e + Ar(i) \rightarrow Ar(j) + e$ Where $i = 1s_2, 1s_3, 1s_4, 1s_5 \;\; j = 3s, 4p, 4d$	b
$e + Ar(i) \rightarrow Ar(4p) + e$ Where $i = 1s_2, 1s_3, 1s_4, 1s_5$	b
$e + Ar(i) \rightarrow Ar^+ + e + e$ Where $i = 1s_2, 1s_3, 1s_4, 1s_5$	b
$e + Ar(j) \rightarrow Ar(i) + e$ Where $i = 1s_2, 1s_3, 1s_4, 1s_5 \; ; j = 4p, 4d$	b
$e + Ar(j) \rightarrow Ar(3s) + e$ Where $j = 4p, 4d$	b
$e + Ar(j) \rightarrow Ar^+ + e + e$ Where $j = 3s, 4p, 4d$	b

b denotes the reaction rate,are calculated within HPEM as part of EETM module. The reaction rates have the following units (1st order : (1/s) ; 2nd order : (cm^3/s); 3rd order : (cm^6/s)).

Table A.2: Heavy Particle reactions

Reactions	Reaction Rate
$e + e + Ar^+ \rightarrow Ar(1s5) + e$	$5.0 * 10^{-27} T_e^{-4.5}$
$e + Ar^+ \rightarrow Ar(1s5)$	$4.0 * 10^{-13} T_e^{-0.5}$
$Ar(1s4) \rightarrow Ar(3s)$	$1.5 * 10^7$
$Ar(1s2) \rightarrow Ar(3s)$	$2.0 * 10^6$
$Ar(4p) \rightarrow Ar(4s)$	$1.0 * 10^6$
$Ar(4p) \rightarrow Ar(1s5)$	$4.0 * 10^6$
$Ar(4p) \rightarrow Ar(1s3)$	$1.6 * 10^7$
$Ar(4p) \rightarrow Ar(1s2)$	$9.3 * 10^6$
$Ar(4d) \rightarrow Ar(1s5)$	$8.5 * 10^6$
$Ar(4d) \rightarrow Ar(1s4)$	$2.0 * 10^5$
$Ar(4d) \rightarrow Ar(1s3)$	$2.0 * 10^5$
$Ar(4d) \rightarrow Ar(1s2)$	$2.0 * 10^5$
$Ar(4d) \rightarrow Ar(4p)$	$2.0 * 10^5$
$Ar_2^* \rightarrow Ar(3s) + Ar(3s)$	$1.0 * 10^7$
$Ar(1s5) + Ar(3s) \rightarrow Ar(1s4) + Ar(3s)$	$1.5 * 10^{-15} \left(\frac{T_g}{300}\right)^{0.5} e^{\frac{-881.2}{T_g}}$
$Ar(1s4) + Ar(3s) \rightarrow Ar(1s5) + Ar(3s)$	$2.5 * 10^{-15} \left(\frac{T_g}{300}\right)^{0.5}$
$Ar(1s5) + Ar(3s) \rightarrow Ar(1s3) + Ar(3s)$	$0.5 * 10^{-15} \left(\frac{T_g}{300}\right)^{0.5} e^{\frac{-2029}{T_g}}$
$Ar(1s3) + Ar(3s) \rightarrow Ar(1s5) + Ar(3s)$	$2.5 * 10^{-15} \left(\frac{T_g}{300}\right)^{0.5}$
$Ar(1s5) + Ar(3s) \rightarrow Ar(1s2) + Ar(3s)$	$1.5 * 10^{-15} \left(\frac{T_g}{300}\right)^{0.5} e^{\frac{-3246}{T_g}}$
$Ar(1s2) + Ar(3s) \rightarrow Ar(1s5) + Ar(3s)$	$2.5 * 10^{-15} \left(\frac{T_g}{300}\right)^{0.5}$

$Ar(1s4) + Ar(3s) \rightarrow Ar(1s3) + Ar(3s)$	$0.83 * 10^{-15} \left(\frac{T_g}{300}\right)^{0.5} e^{\frac{-1148}{T_g}}$
$Ar(1s3) + Ar(3s) \rightarrow Ar(1s4) + Ar(3s)$	$2.5 * 10^{-15} \left(\frac{T_g}{300}\right)^{0.5}$
$Ar(1s4) + Ar(3s) \rightarrow Ar(1s2) + Ar(3s)$	$2.5 * 10^{-15} \left(\frac{T_g}{300}\right)^{0.5} e^{\frac{-2365}{T_g}}$
$Ar(1s2) + Ar(3s) \rightarrow Ar(1s4) + Ar(3s)$	$2.5 * 10^{-15} \left(\frac{T_g}{300}\right)^{0.5}$
$Ar(1s3) + Ar(3s) \rightarrow Ar(1s2) + Ar(3s)$	$7.5 * 10^{-15} \left(\frac{T_g}{300}\right)^{0.5} e^{\frac{-1217}{T_g}}$
$Ar(1s2) + Ar(3s) \rightarrow Ar(1s3) + Ar(3s)$	$2.5 * 10^{-15} \left(\frac{T_g}{300}\right)^{0.5}$
$Ar(i) + Ar(j) \rightarrow Ar^+ + Ar(3s) + e$ Where $i, j = 1s_2, 1s_3, 1s_4, 1s_5, 4p, 4d$	$1.2 * 10^{-9} \left(\frac{T_g}{300}\right)^{0.5}$
$Ar^+ + Ar(3s) \rightarrow Ar(3s) + Ar^+$	$5.66 * 10^{-10} \left(\frac{T_g}{300}\right)^{0.5}$
$Ar(i) + Ar(3s) + Ar(3s) \rightarrow Ar_2^* + Ar(3s)$ Where $i = 1s_2, 1s_3, 1s_4, 1s_5, 4p, 4d$	$1.14 * 10^{-32} \left(\frac{T_g}{300}\right)^{-1}$
$Ar(i) + Ar(j) \rightarrow Ar_2^+ + e$ Where $i, j = 1s_2, 1s_3, 1s_4, 1s_5, 4p, 4d$	$5.70 * 10^{-10} \left(\frac{T_g}{300}\right)^{0.5}$
$Ar(4d) + Ar(3s) \rightarrow Ar_2^+ + e$	$2.0 * 10^{-9} \left(\frac{T_g}{300}\right)^{0.5}$
$Ar^+ + Ar(3s) \rightarrow Ar(1s5) + Ar(3s)$	$2.5 * 10^{-31} \left(\frac{T_g}{300}\right)^{-1}$
$Ar_2^* + Ar_2^* \rightarrow Ar_2^+ + Ar(3s) + Ar(3s) + e$	$5.0 * 10^{-10} \left(\frac{T_g}{300}\right)^{0.5}$
$e + Ar_2^+ \rightarrow Ar(3s) + Ar(1s5)$	$2.69 * 10^{-8} (T_e)^{-0.66}$
$e + Ar_2^+ \rightarrow Ar(3s) + Ar(3s)$	$2.69 * 10^{-8} (T_e)^{-0.66}$
$e + Ar_2^* \rightarrow Ar_2^+ + e + e$	$9.0 * 10^{-8} (T_e)^{0.70} e^{\frac{-3.66}{T_e}}$
$e + Ar_2^* \rightarrow Ar(3s) + Ar(3s) + e$	$1.0 * 10^{-7}$

APPENDIX B. LIST OF Ar-H_2O REACTIONS

Argon-water vapor mixture involves reactions of argon in Appendix A and additional reactions of Ar with H_2O are implemented in the HPEM code. It has been observed that HPEM includes all the electron impact reactions of the species included in the reaction data set despite specifying only a few required reactions. [21] [22] [23]

The additional species we included in the data set for modeling the argon-water mixture are as follow, H, H_2, OH, H_2O, H_2O^+, H_3O^+, and ArH^+. HPEM has a defined set of electron impact reactions hard coded. So, the following electron impact reactions of the species specified are forced by HPEM to include in our calculations.

Table B.1: Electron impact reactions

Reactions	Reaction Rate
$e + ArH^+ \rightarrow ArH^+ + e$ (momentum transfer)	b
$e + ArH^+ \rightarrow Ar + H$	b
$e + H_2O \rightarrow H_2O + e$ (momentum transfer)	b
$e + H_2O \rightarrow H_2O(100) + e$ (Vibrational excitation)	b
$e + H_2O \rightarrow H_2O(010) + e$ (Vibrational excitation)	b
$e + H_2O \rightarrow H_2O(001) + e$ (Vibrational excitation)	b
$e + H_2O \rightarrow H^- + OH + e$	b
$e + H_2O \rightarrow O^- + H_2 + e$	b
$e + H_2O \rightarrow OH^- + H + e$	b
$e + H_2O \rightarrow H + OH + e$	b
$e + H_2O \rightarrow O + 2H + e$	b
$e + H_2O \rightarrow H_2O^+ + e + e$	b
$e + H_2O \rightarrow OH^+ + H + e$	b
$e + H_2O \rightarrow O^+ + 2H + 2e$	b

$e + H_2O \rightarrow H_2^+ + O + e$	b
$e + H_2O \rightarrow H^+ + OH + 2e$	b
$e + H_2O \rightarrow H + OH^* + e$	b
$e + H_2O \rightarrow H^* + OH + e$ $H^* = H(2)\ [\ 121.6nm\ ]$	b
$e + H_2O \rightarrow H^{**}(3)\ + OH + e$ $H^{**} = H(3)\ [\ 656.3nm\ ]$	b
$e + H_2O \rightarrow H^{***} + OH + e$ $H^{***} = H(4)\ [\ 486.1nm]$	b
$e + H_2O \rightarrow O(3p5p)\ [\ 777.4nm\ ] + H_2 + e$ $O^{****} = O(3p5p)\ [\ 777.4nm\ ]$	b
$e + H_2O^+ \rightarrow H_2O^+ + e$ (momentum transfer)	b
$e + H_2O^+ \rightarrow H_2O + e$	b
$e + H \rightarrow H + e$ (momentum transfer)	b
$e + H \rightarrow H^* + e$	b
$e + H \rightarrow H^{**} + e$	b
$e + H \rightarrow H^{***} + e$	b
$e + H \rightarrow H^+ + e$	b
$e + H_2 \rightarrow H_2 + e$ (momentum transfer)	b
$e + H_2 \rightarrow H_2(r1) + e\ \ \{r1 = Rotational(0-2)\}$	b
$e + H_2 \rightarrow H_2(r2) + e\ \ \{r2 = Rotational(1-3)\}$	b
$e + H_2 \rightarrow H_2(v1) + e\ \ \{v1 = vibrational\ state\}$	b
$e + H_2 \rightarrow H_2(v2) + e\ \ \{v2 = vibrational\ state\}$	b
$e + H_2 \rightarrow H_2^* + e\ \ \{H_2^* = H_2(b3\ \Sigma)\}$	b
$e + H_2 \rightarrow H_2^* + e\ \ \{H_2^* = H_2(c3\ \Pi)\}$	b

$e + H_2 \rightarrow H_2^+ + e$	*b*
$e + H_2 \rightarrow H + H$	*b*
$e + H_2 \rightarrow H^*(\alpha) + H + e$	*b*
$e + OH \rightarrow OH + e$ (momentum transfer)	*b*
$e + OH \rightarrow OH(v1) + e \ \ \{v1 = vibrational\ state\}$	*b*
$e + OH \rightarrow OH(a1\Pi) + e$	*b*
$e + OH \rightarrow O + H + e$	*b*
$e + OH \rightarrow OH(c1\Sigma) + e$	*b*
$e + OH \rightarrow OH(e1\Pi) + e$	*b*
$e + OH \rightarrow OH(b1\Sigma) + e$	*b*
$e + OH \rightarrow OH(i1\Sigma) + e$	*b*
$e + OH \rightarrow OH(d1\Delta) + e$	*b*
$e + OH \rightarrow OH(a3\Pi) + e$	*b*
$e + OH \rightarrow OH(a3\Sigma) + e$	*b*
$e + OH \rightarrow OH(d3\Delta) + e$	*b*
$e + OH \rightarrow OH(e3\Sigma) + e$	*b*
$e + OH \rightarrow OH^+(x2\Sigma) + e + e$	*b*
$e + OH \rightarrow OH^+(a2\Pi) + e$	*b*
$e + OH \rightarrow OH^+(b2\Sigma) + e + e$	*b*
$e + OH \rightarrow H^+ + O + e + e$	*b*
$e + OH \rightarrow O^+ + H + e + e$	*b*
$e + OH \rightarrow OH^+ + e + e$	*b*

b denotes the reaction rate coefficients are calculated within HPEM as part of EETM module.

Table B.2: Heavy Particle reactions

Reactions	Reaction Rate
$e + H_2O^+ \rightarrow H_2O$	$12.55 * 10^{-8} T_e^{-0.5}$
$e + H_3O^+ \rightarrow H_2O + H$	$9.9 * 10^{-8} T_e^{-0.7}$
$H_2O + H_2O^+ \rightarrow H_3O^+ + OH$	$1.85 * 10^{-9}$
$H_3O^+ + OH \rightarrow H_2O + H_2O^+$	$1.30 * 10^{-9}$
$Ar^+ + H_2O \rightarrow Ar(3s) + H_2O^+$	$7.0 * 10^{-10}$
$Ar(3s) + H_2O^+ \rightarrow Ar^+ + H_2O$	$1.5 * 10^{-10}$
$Ar^+ + H_2O \rightarrow ArH^+ + OH$	$1.31 * 10^{-9}$
$ArH^+ + H_2O \rightarrow Ar(3s) + H_3O^+$	$4.90 * 10^{-9}$
$Ar_2^+ + H_2O \rightarrow H_2O^+ + 2Ar(3s)$	$1.65 * 10^{-9}$
$Ar(4p) + H_2O \rightarrow H_2O^+ + Ar(3s) + e$	$6.60 * 10^{-10}$